

Mechanochromic Suction Cups for Local Stress Detection in Soft Robotics

Goffredo Giordano,* Rob Bernardus Nicolaas Scharff, Marco Carlotti, Mariacristina Gagliardi, Carlo Filippeschi, Alessio Mondini, Antonio Papangelo, and Barbara Mazzolai*

Advancements in smart soft materials are enhancing the capabilities of robotic manipulators in object interactions and complex tasks. Mechanochromic materials, acting as lightweight sensors, offer easily interpretable visual feedback for localized stress detection, structural health monitoring, and energy-efficient robotic skins. Herein, an innovative mechanochromic soft end-effector capable of discerning local contact stresses during mechanical interactions with objects is presented and their relative position is ascertained. This system utilizes a reversible force-induced color switch in a thin layer of spiropyran-functionalized polydimethylsiloxane, which coats a silicone-made suction cup. The mechanochromic suction cup is integrated with a 3D-printed compact load-transferring system and electronic color-changing detection elements. The assembly may serve as a synthetic receptor for robotic actuators, discerning localized interaction forces down to 3 N. The system's resilience to varying environmental factors, including illumination, tilting, and interaction with objects of various shapes is verified. The results indicate potential for exteroceptive solutions in reconfigurable manipulation tasks without compromising the overall softness of the manipulator.

1. Introduction

Soft robots with intelligent end-effectors that can accurately discern tactile interactions and enhance dexterity are yet lacking.^[1] This limits their widespread application in various domains like human-machine interaction, medical devices, wearables, and exploratory robotics.^[2–4] To address this gap, there is an urgent need for stretchable, fully embedded, and stable exteroceptive sensors that seamlessly integrate with the manipulator, enabling adaptability, safe execution, and enhanced dexterity.^[5,6]


Stimuli-responsive smart materials have the potential to provide soft robotic manipulators with real-time information regarding the force, stiffness, and pressure distribution exerted on objects.^[7–10] The possibility of integrating, either by physical dispersion or chemical bonding, functional and responsive units in structural bio-/polymers and hydrogels is appealing for

robust exteroceptive sensors, responsive structural joints, and actuators.^[11–13] They can act as both constitutive and sensing elements, enhancing bodily awareness of soft manipulators,

G. Giordano, R. B. N. Scharff, C. Filippeschi, A. Mondini, B. Mazzolai
Bioinspired Soft Robotics
Istituto Italiano di Tecnologia (IIT)
16163 Genova, Italy
E-mail: goffredo.giordano@iit.it; barbara.mazzolai@iit.it

G. Giordano, A. Papangelo
Department of Mechanics Mathematics and Management
Politecnico di Bari
70126 Bari, Italy

R. B. N. Scharff
Division of Integrative Systems and Design
The Hong Kong University of Science and Technology
Clear Water Bay, Hong Kong, China

 The ORCID identification number(s) for the author(s) of this article can be found under <https://doi.org/10.1002/aisy.202400254>.

© 2024 The Author(s). Advanced Intelligent Systems published by Wiley-VCH GmbH. This is an open access article under the terms of the Creative Commons Attribution License, which permits use, distribution and reproduction in any medium, provided the original work is properly cited.

DOI: 10.1002/aisy.202400254

M. Carlotti
Center for Materials Interfaces
Istituto Italiano di Tecnologia (IIT)
56025 Pontedera, Italy

M. Carlotti
Dipartimento di Chimica e Chimica Industriale
University of Pisa
56126 Pisa, Italy

M. Gagliardi
NEST
Istituto Nanoscienze-CNR and Scuola Normale Superiore
56126 Pisa, Italy

A. Papangelo
Department of Mechanical Engineering
Hamburg University of Technology
Am Schwarzenberg-Campus 1, 21073 Hamburg, Germany

and serving as communicative signals of the robot's state, easily detectable by human senses, thereby facilitating a higher level of interaction.^[14,15] Mechanochromism, i.e., the change of color of a material in response to a mechanical stimulus, is a prominent example of this kind of responsiveness, which has gathered a growing interest over the past decades.^[16,17] One promising approach involves embedding mechanophores in polymeric matrices, such as those constituting components of soft robots without hindering their mechanical properties,^[18,19] while enabling an external stress to trigger a measurable and reversible color (or fluorescence) change.^[20–27] This innovative approach allows for the development of lightweight force/pressure devices fully embedded into the robotic skin, with an easy-to-read visual cue feedback during grasping, and manipulation.^[28,29] The mechanically induced optically reactive behavior has been exploited in camouflaging soft robots^[30–33] and adaptive displays in smart skin technologies,^[34–36] taking cues from organisms such as cephalopods, that exhibit fast adaptive color-changing capabilities.^[37,38] Further biological studies on these animals can inspire devices correlating grade of touch^[39] and mechanically driven color changing (e.g., devices for real-time feedback of structural damage,^[40] optomechanical electronics,^[41] triboelectric and piezochromic nanogenerators,^[42,43] and adaptive energetic harvesters^[44–46]). Alternatively, the soft robotics community is investigating other exteroceptive sensing approaches like innovative stretchable strain and force sensors,^[47] or magnetic,^[48,49] or based on signal lossy optical waveguides^[50] or wavelength-shift,^[51] that can determine various parameters such as proximity, contact, direction, imbalance, and weight of the objects to be gripped.^[52–55] Overall, factors such as compliance, spatial resolution, robustness, stability, simple readout, and integration that do not compromise the softness of the manipulator require consideration.^[56]

In our study, we tackle a crucial challenge involving mechanochromic materials as exteroceptive sensors fully integrated in a soft end-effector. Our solution addresses the need to detect intricate events, like the end-effector's relative orientation, or the force applied for a safe and gentle manipulation, by ensuring that 1) mechanochromic activation occurs only when relevant events happen (i.e., colorimetric on/off switch); and 2) the localized color change can be reliably detected through electronic sensors embedded within the end-effector structure. We fabricate a thin layer of polydimethylsiloxane (PDMS) functionalized with a spiropyran-based mechanochromic dye (SP) to coat the suction cup end-effector, resulting in a mechanochromic-coated suction cup (MSC). We decide to employ this particular system as PDMS is an elastomer characterized by suitable mechanical properties, which can be obtained with high reproducibility employing simple fabrication procedures, and high optical transparency, thus allowing for a clear observation of any color change. The covalent modification of the PDMS matrix with SP units makes the system mechanochromic as, upon application of a mechanical stimulus, the SP units can isomerize to their merocyanine form, thus changing the color of the PDMS from yellow to deep purple in a reversible manner.^[57] The color-changing is detected by three digital color sensors (DCS) integrated into a compact frame with three indenters arranged at 120° each apart, which are positioned above the mechanochromic end-effector. The indenters are responsible for triggering the mechanochromism at the

minimum load (≈ 3 N for indenter). Furthermore, they act as cylindrical frames for optical waveguides for color-changing detection (**Figure 1**). When the SP covalently bonded with PDMS layer (SP-PDMS) undergoes color-changing simultaneously at each of the three indenters, we determine the perpendicularity of the MSC with respect to the object. The ability to distinguish perpendicular and tilted contact through differences in the color-changing measurement by the DCS is demonstrated through experiments on flat, curved, sharpened, and inclined surfaces. In view of future applications of the technology in soft robotic arms, it is demonstrated that the MSCs and compact load-transferring and local stress detection system could be easily integrated into a PneuNet robotic manipulator, and deployed for exploring various geometries (curved objects, object edges, etc.).^[58]

By enhancing tactile perception and enabling the handling of unstructured objects, our system may address a crucial challenge that can propel soft robotic systems beyond laboratory settings and into practical applications in various industries and factories, although time responses and integration improvements are yet required.^[59] The ability to perform dexterous manipulation tasks in unstructured environments is particularly important for replacing human work in hazardous and inaccessible settings, such as pipelines, offshore oil and gas environments, and agriculture.^[60,61]

2. Results

We introduce a novel method utilizing mechanochromism (hereinafter referred to as an on/off colorimetric switch due to a mechanical stress) to detect and quantify forces exerted by soft end-effectors during mechanical interaction and assess their relative position to the object. The goal is to provide three distinct points of visible cues that can be detected by the three DCS units housed within a 3D-printed translucent frame. Our solution involves the design, fabrication, and characterization of the MSC assembled with the 3D-printed, durable, watertight, and translucent frame. This frame houses a printed circuit board (PCB) which integrates three DCS equally spaced from the corresponding white light sources (LEDs) in a circular arrangement, as well as three specially designed punch shapes for both detection and load transfer purposes (**Figure 1**, S11, Supporting Information). Punch shape selection is critical for transferring load from a general actuator (e.g., PneuNet, tendon-driven, etc.) to the MSC and initiating/measuring the mechanochromic response. Each indenter directly contacts the mechanochromic thin layer (MTL) coating the dome-like suction cup (**Figure 2A**). Three LEDs emit light onto the MTL, and the DCS exclusively captures the reflected light components (i.e., RGB values). The illumination cone is accurately aligned with the three corresponding load-transferring indenters, which also serve as optical waveguides. The inclusion of three detection points enhances the system robustness in localized stress detection, ensuring reliable performance under varying manipulation task configurations and environmental conditions. To evaluate the system effectiveness in different scenarios, we conduct multiple tests, involving variations in the angle of compression, punch shapes, and ambient lighting conditions, providing

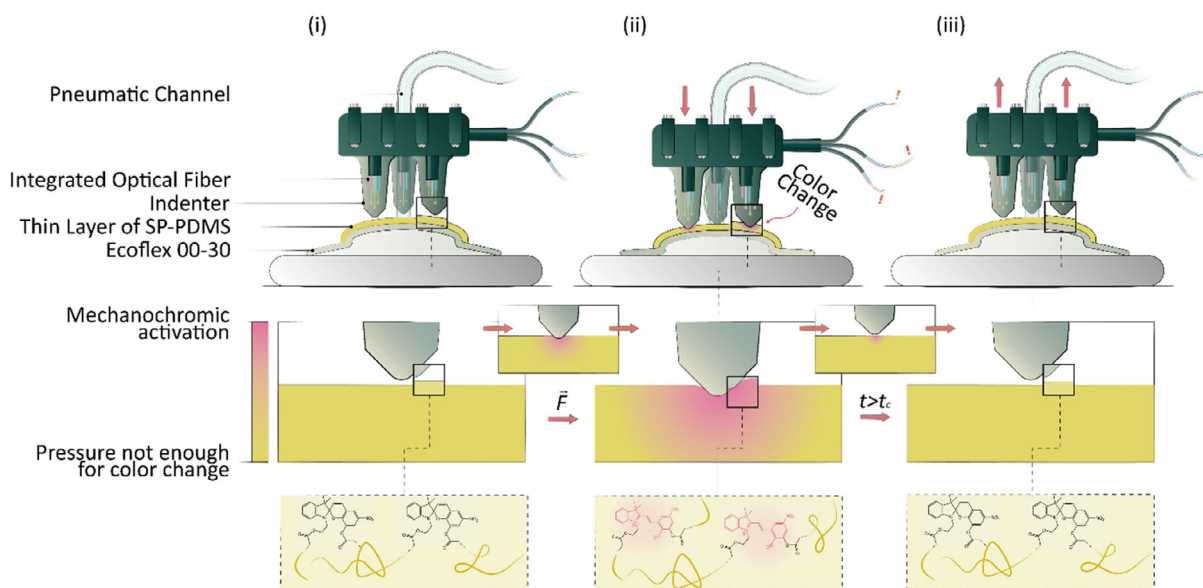


Figure 1. A three-level illustration from the macroscopic to the microscopic and molecular levels (from top to bottom respectively) of the conceived mechanically-induced color-changing detection mechanism integrated into a soft end effector (a soft suction cup coated with a mechanochromic thin layer, MTL). Top level: the load-transferring and local stress detection mechanism consists of a compact frame that houses electronics and indenting elements, which respectively detect and generate color changes on the MTL. The indenters are integrated with optical fibers or filled with microscope optical oil to enhance local color detection from DCS. The sequence from left to right shows: i) the compact frame approaching the MTL. ii) The load-transferring able to reach the mechanochromic activation pressure, inducing local color changes in each respective indented area. iii) The load releasing, with the local color change reversibly fading out within the characteristic time (t_c). Central level: from left to right, the miniaturized replication of the time step events with the color legend (on the left side) provided to help visualize the load-induced mechanochromism and it is fading out within the indented area. Bottom level: from left to right, the molecular-level depiction of the chemical mechanism underlying the mechanically-induced color change in the SP-PDMS thin layer. Within the dashed rectangle, the SP molecule acts as a crosslinker in the PDMS network (represented by bold yellow random lines). The molecule is covalently bonded with two vinyl functional groups, one attached to the benzopyran ring and one to the indoline ring at the N-position. Macroscopic load translates into the stretching of the polymeric chains, inducing the reassembly and stretching of the complex SP-PDMS system. This results in the breaking of the spiro C–O bond and the transformation from the colorless SP species to the colored and planar blue/violet merocyanine form. Upon releasing the macroscopic load, the polymeric chains return to a more energetically stable condition, reverting to the SP species and resulting in a reversible, thermodynamically dependent mechanochromic phenomenon within its t_c .

valuable insights into the performance and capabilities of the proposed system.

2.1. The Design and Fabrication of the Color-Changing and Force-Responsive Suction Cup and Its Detection System

The main component in contact with the substrate or object to be manipulated is the dome-like suction cup, which is fabricated using an elastomeric material (Ecoflex00-30, Smooth-On, $E = 0.32 \pm 0.01$ MPa) and coated with a thin layer of PDMS (Sylgard184) functionalized with mechanochromic spiropyran units (SP-PDMS), to confer force-responsive properties and material intelligence (Figure 2A). The MTL is composed of a PDMS matrix with a prepolymer/curing agent ratio of 2.5:1% and 2% wt of the small molecule SP which is opportunely functionalized to crosslink in with the siloxane chains (Experimental Section). We adopted such formulation as, from previous studies, it exhibits the lowest mechanochromic activation pressure, specifically 1.17 ± 0.25 MPa (Figure S12, Supporting Information).^[62] The inherent properties of Ecoflex00-30 enable the effector to be highly flexible and adaptable when compressed under the load transferred from the actuator. The suction cup

design features a simplified structure, consisting of a dome-like and semicircular body with a diameter of 11 ± 0.01 mm, an averaged thickness of 3.50 ± 0.30 mm, along with the MTL. The mechanical properties of the different silicone matrices are detailed in Table S11, Supporting Information. The MTL (average thickness of 0.65 ± 0.08 mm) is bonded at 90°C for 3 h on top of the Ecoflex00-30 body. It appears yellowish in stable conditions and can reversibly switch to bluish/violet when the mechanochromism is triggered. The MSC is endowed with a coaxial silicone-made pneumatic tube, which generates suction with pneumatic actuation when the acquisition system detects the color change of the MTL (occurring when a sufficient mechanical load is reached), and the perpendicularity of the end-effector to the object.

In-built with the MSC, there are the load transfer and color detection system. The casing of the system is 3D-printed with a stereolithography printer (SLA, FormLabs 2), adopting a translucent and stiff photopolymer (Clear Resin, FormLabs, $E = 2.6$ GPa). The design includes three indenters (120° each apart) with different punch forms and allows the pneumatic tube to pass through it coaxially (Figure 2B). The presence of three indenters enables multipoint detection to exploit the

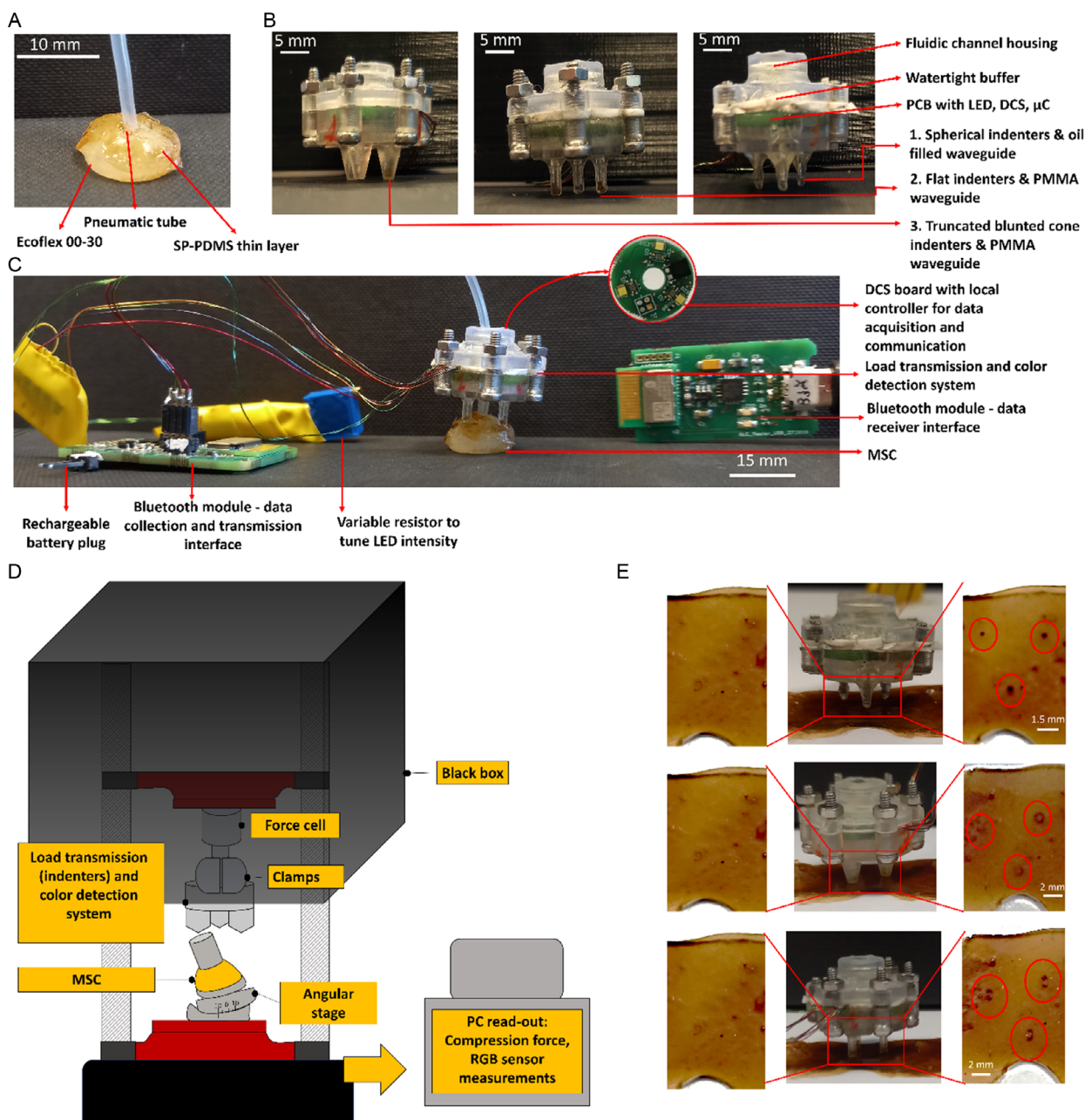


Figure 2. A) The MSC prototype comprises an Ecoflex00-30 dome-like body coated with a yellowish SP-PDMS thin layer and integrated with a concentric pneumatic tube for actuation upon reaching the desired compression load and perpendicularity to the grasped object. B) From left to right, the 3D-printed frames with truncated blunted conical-, planar-, and spherical-shape indenters for localized stress detection and mechanochromic activation. These frames include compartments for electronics (PCB with LED, DCS, and integrated circuits) communicating data via Bluetooth, and their shape-variable indentation elements house optical fibers or fluidic waveguides to optimize optical coupling with DCS. Concentric within the frames there is the housing for the fluidic channel for potential MSC actuation. C) In the middle, the MSC in-built with the 3D-printed frame with cylindrical indenters. On the left, there is the Bluetooth module, data collector, and transmission interface, that is powered by a 5 V rechargeable battery. This module is connected with the PCB board and drives the required amount of current to turn-on LED and feeding DCS. A variable resistor bridges LED and electrical source to tune the light intensity to optimize color detection. On the top right, the inset shows the circular PCB, accommodating LED, DCS, and microcontroller for data acquisition and communication. On the right, the Bluetooth module and data receiver interface are able to communicate with the PC by USB communication port. D) The illustrated optomechanical setup is a UTM, where the 3D-printed frame with DCS board and indenters is clamped and directly connected to the force cell. The compression experiment is controlled by a PC that also acquires data. The frame acts on the MSC, or MTL, laying on a goniometric stage that is allowed to rotate at different angular positions. In case of simulated dark condition experiments, a black box is allowed to cover the entire UTM neglecting ambient light to reach the experimental stage. E) From left to right, the MTL in its stable (yellowish) condition, under load, and after compression (localized bluish/violet regions), respectively. From top to bottom, indentation is performed by spherical-, truncated blunted conical-, and flat-shape indenters, respectively.

morphological adaptation and conformability of the MSCs to the counter-surface. The optical properties of the 3D-printed material play a crucial role in facilitating optical coupling between the DCS and the localized color-changing region. Indeed, the different typologies of indenters (i.e., tip shapes as spherical, flat, and blunted cones) act both as force-transferring elements and as optical waveguides. Each indenter shape is investigated both theoretically and experimentally to analyze the load-transferring to the object, and consistently triggers the mechanochromism at a particular localized stress threshold. The frame is 3D-printed in two parts to facilitate the subsequent mounting of the PCB and integrate it with a watertight buffer made of polymeric material (Polyester Mylar A). The latter enables the adoption of the system in harsh or fluid-filled environments.

The spherical terminations (radius of 0.50 ± 0.03 mm) are printed with Clear Resin separately and manually postglued at the tubular indenting terminations, due to printing limitations. The top part of the frame features a circular element with a concentric hole for the fluidic channel and the PCB wiring connections to the external microcontroller. External inserts are also included to enable screwing and tightening of the frame (Figure S13, Supporting Information). The bottom part is designed to accommodate the PCB and the embossed elements (DCS and LED), with the DCS positioned along the axis of the indenters (Figure S11, Supporting Information). All indenters maintain a height of 5.00 ± 0.01 mm, ensuring a minimum optical path and working distance between the DCS and the color-changing region. This working distance balances optical coupling requirements with ensuring effective load transfer from the indenter tip to the MSC without contacting the sensor housing. However, it significantly affects the sensitivity of DCS. Thus, to improve the retro-reflection light acquisition of the DCS, the tubular structures of the spherical indenters are filled with microscope optical oil (Immersion Oil Immersol 518F), acting as a liquid waveguide with increased numerical aperture. Furthermore, the sensitivity of the DCS is electronically enhanced to maximize the detection of RGB components with a fixed illumination from each white LED (Experimental Section). Then, the top and bottom parts are assembled and screwed together.

The same assembly procedure is followed for the flat-based and the blunted cone-based detection and indentation systems. The flat-based indenter features a hollow cylindrical shape with a 5.00 ± 0.01 mm height and a contact radius of 0.50 ± 0.02 mm. The optical paths of the cylindrical indenters are filled with 5.0 ± 0.2 mm length pieces of PMMA-based bare optical fibers (0.5 mm diameter), which are in direct contact with the DCS to enhance the detection of color changes. The blunted cone indenters (cone-half angle $\theta = 20^\circ$) have a smoothed truncation with an internal diameter opening of 1.00 ± 0.02 mm, accommodating 5.0 ± 0.2 mm length pieces of PMMA-based optical fibers (0.5 mm diameter). The length of the optical path is consistently maintained at 5.0 ± 0.1 mm.

In Figure 2C, we show the load transferring and color detection system with the electronics required to convert the color percentage variation (i.e., the blue-to-red color component) and correlate it to the compression force exerted. The detection system is an electronic board that acquires and transfers the data from each DCS through an I2C (Inter Integrated Circuit) communication protocol to the data acquisition board that packs

them and sent wirelessly through Bluetooth communication to a twin Bluetooth module allowing the data to be processed by the PC.

2.2. Optomechanical Characterization of the Color-Changing and Force-Responsive Thin Layer

To achieve a reliable force-detection system for a generic robotic manipulator, we conduct a comprehensive characterization of the MTL subjected to mechanical compression using different punch shapes, varying compression angles, and different environmental light conditions. In Figure 2D, we report the experimental optomechanical setup whose test procedures are explained in detail in the Experimental Section. The adopted electrical circuit parameters (overall forward driving current DCS ≈ 201.7 μ A) avoid reaching the response saturation of the DCS during compression tests. The setup involves clamping the DCS housing frame, along with the corresponding indenter shapes, to a universal testing machine (UTM) and connecting it to a force cell (50 N). The electronic colorimetric sensing devices are directly connected by a Bluetooth module to the PC-readout, enabling real-time acquisition of RGB components. During the compression tests, both for the MTL and the MSC on a rigid substrate, we apply predetermined compression force steps (e.g., 0, 5, 10, 13, and 16 N), and consistently we record the corresponding RGB values at each time steps, both in ambient light and dark conditions (a black box is used to simulate dark condition), while the tilting angle condition is achieved by using a goniometer stage. Figure 2E shows the MTL in its stable condition (left), and after triggering the mechanochromism (right) under compression applied from the different punch shapes (center). The color-changing footprints are highlighted by red circles, and they trace what the embedded electronic system may detect.

In Figure 3, we present the experimental data, illustrating the correlation between color-changing detection and the exerted compression force during the indentation of the MTL laying on a steel substrate adopting three spherical punches at 120° each apart. The tests are conducted under ambient and dark light, and varying tilting angles (0° , 10° , 20° , and 30°). The data are collected for at least three repetitions of the same 3D-printed frame endowed with the respective three shape variable punches, and each bar represents the average of three attempts for each indenting force (Experimental Section). The color change detection is represented by the ratio of the blue-to-red component recorded at each time step by the DCS. We consider blue-to-red component ratio because the activation of the mechanophore produces an absorption band centered at around 590 nm which is not present in its initial state (Figure S14, Supporting Information). All the data and error bars are reported in averaged percentage variation, normalizing respect to 0 N acquisition. The latter corresponds to the most proximal position between the indenter tips and the MTL (i.e., steady state). The indenter is considered to have successfully detected a color change and its respective force-threshold if, considering its lowest value of the error bar (σ_1) of the average value (μ_1) of the channel (i.e., #1, #2, #3), this is still higher than the highest value of the relative error bar at 0 N (σ_2 , μ_2). This is called force-threshold confidence detection condition (FC). In statistical terms, we refer to

Spherical punch on SP-PDMS thin layer on a steel substrate

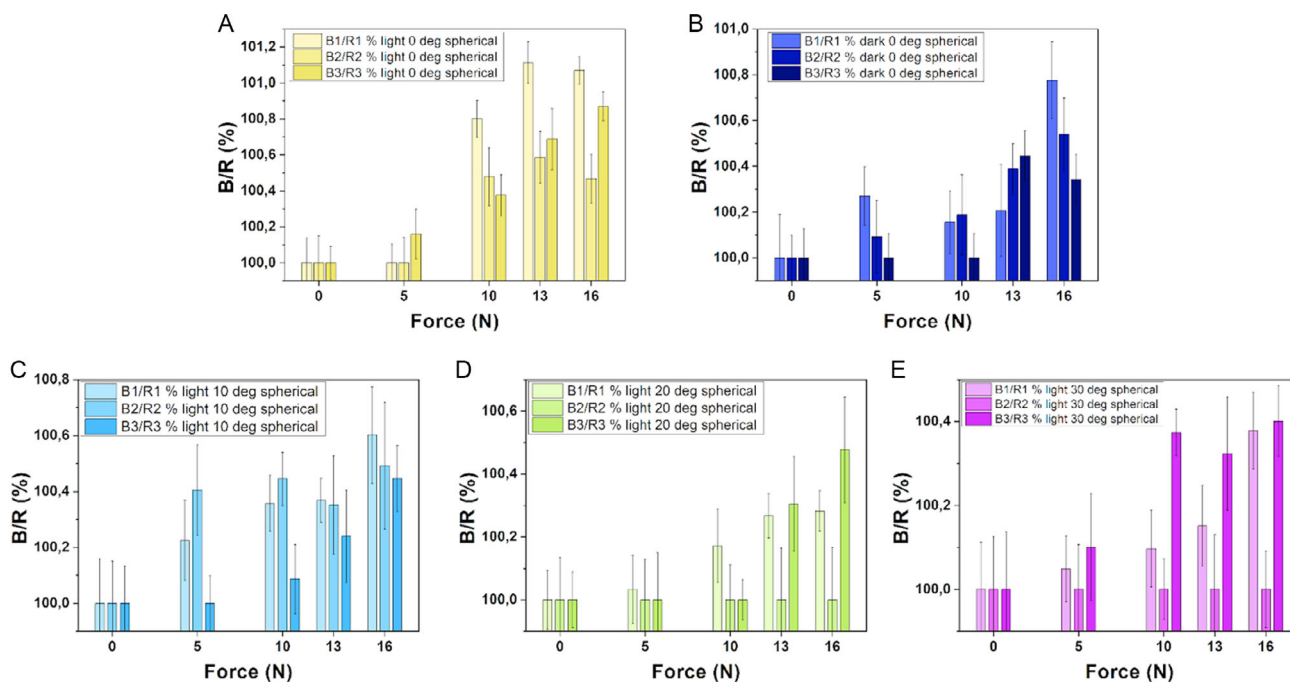


Figure 3. Experimental characterization of three spherical punch shapes on a thin SP-PDMS layer laying on a steel substrate. Variable conditions are enlightenment and tilting angle between punch shapes and mechanochromic sample. All data are reported with their standard deviation, and the bar values at each compression force values are the average of the blue-to-red component for three acquisitions for each channel, rescaled in percentage variation. A) Indentation in ambient light conditions at 0° tilting angle. Pale yellow is related to the #1 indenter, in yellow is highlighted the #2 indenter, while in dark yellow it is reported the #3 indenter. Hereinafter, all results labeled as indenter #1, #2, and #3 correspond to the respective DCS. For the criteria adopted for perpendicularity and force detection, all the channels are activated homogeneously at 10 N. B) Indentation at 0° tilting angle in dark conditions. Pale blue relates to #1 spherical indenter, blue is for #2, and dark blue for #3. Robust detection is at 16 N, where the activation is homogeneous, and the surface is detected as not inclined by the sensing system. C) Indentation at 10° under ambient light conditions. Pale turquoise is #1, turquoise is #2, and dark turquoise is #3. The force threshold detection is at 10 N, and the homogeneous color activation arises at #1 and #2 locations. Further compression until 16 N may return a perpendicular information about relative position between the indenter and the stimuli-responsive layer. D) Indentation at 20° under light conditions. Pale green is #1, green is #2, and dark green is #3. #1 and #3 detect homogeneously at 13 N the inclined surface. Compressing at overall 16 N, #2 is yet not in contact or not generates enough localized pressure to induce mechanochromism, thus the system reports reliable physical information about inclination and force detection. E) Indentation at 30° under light conditions. Pale purple is #1, purple is #2, and dark purple is #3. #1 and #3 return reliable information about interaction with an inclined surface with an exerted compression force detected at 16 N. Thus, #2 is never in contact with the inclined sample in the experimental campaign.

FC by analyzing the cumulative distribution functions (CDF) as detailed in Experimental Section. We define that a reliable force-threshold detection occurs when the probability of the complement of the CDF is higher than 30%. If this probability is between 10% and 30% then the system is likely detecting an inclined surface (i.e., inclined confidence criterion), otherwise if the probability is less than 10%, there is no detection. Thus, the inclined confidence criterion (IC) returns physical information about the number of indenters able to be in contact and reliably trigger the mechanochromism, and from this parameter, we can derive information on the spatial configuration of the MTL with respect to counter-surfaces. Then, we define criteria to identify 1) the perpendicularity/tilting; and 2) the minimum force-threshold applied and detected to the encountered object. If the three spots are homogeneously colored and detected (i.e., sufficient load achieved), we can assure a reliable perpendicular interaction with a robust force-feedback system. However, the IC/FC are experimentally highly dependent on optical coupling

(e.g., fabrication and assembly issues), DCS sensitivity (e.g., slight clamping misalignment), electronics-related factors (e.g., integration time, forward driving current), punch shape (e.g., manual gluing), and misalignment between the indenters' casing and the MTL, that may cause false-negative. These premises for data analyses are to be considered in every experiment along the text.

Figure 3A presents the results obtained under ambient light conditions at a 0° tilting angle. At a force threshold of 10 N, DCS#1, #2, and #3 each detect a significant local color change on the MTL due to stresses induced by spherical punches. The localized stress required to trigger mechanochromism for each indenter is ≈ 3 N. The IC criterion returns that the interaction acts perpendicularly on a flat surface, and the overall stress transferred is around 10 N (Figure S15(2), Supporting Information). However, in Figure 3A, there could be an ambivalence because of a spike for DCS#3 also at 5 N indentation force, but the overlap of the error bars between the steady-state and the

presumed activated spot may suggest a false positive signal (i.e., FC criterion). Figure 3B shows results in dark condition. At about 16 N, the load triggers the mechanochromism over all the three indenters, so that the IC returns information for a perpendicular condition and the FC for a reliable force-detection. In Figure 3C, the experiments at 10° under ambient light conditions return a reliable overall force-threshold detection at 10 N for DCS#1 and #2 (FC > 30%), while results related to DCS#3 show that 10% < FC < 30%, thus, we can conclude that the system is interacting with an inclined surface (Figure SI5(2), Supporting Information). At 20° with enlighten condition, DCS#1 and #3 detect an overall compression force of 13 N, while DCS#2 returns no detection (FC < 10%). This condition may suggest that the two activated spots are aligned in the same direction as the angular goniometric stage orientation, while DCS#2 is likely not in contact with the surface (Figure 3D, SI5(2), Supporting Information). The same may be inferred at 30° with an overall force detection of 16 N and an inclination condition (Figure 3E, SI5(2), Supporting Information).

In Figure 4, we examine the interaction of flat punches with the MTL positioned on smooth, flat counter-surfaces at various tilting angles under ambient light. Figure 4A demonstrates that each DCS detects ≈6 N when interacting with a steel surface tilted at 0°, resulting in an overall mechanochromic activation force threshold of 18 N (Figure SI5(2), Supporting Information). However, according to the inclination criterion, this interaction is classified as an inclined surface, leading to a false-negative detection. Figure 4B shows that at a tilting angle of 10°, the system uniformly detects mechanochromic activation at 15 N, indicating interaction with a flat surface (Figure SI5(2), Supporting Information). Nevertheless, this sensory feedback does not match the physical results observed in the experiments. In contrast, Figure 4C accurately reports interactions with a

surface tilted at 20°, with an overall force-threshold detection at 18 N (Figure SI5(2), Supporting Information). Here, DCS#1 detects the mechanochromic color change with over 40% confidence, DCS#3 identifies an inclined surface, while DCS#2 shows no signal, suggesting it may not be in contact and supporting the real conditions of the experimental characterization.

The lower percentage variation between steady-state and mechanically perturbed conditions for all indenters, along with the higher variability (i.e., standard deviation) in measurements from the flat indenters, may be attributed to optical path manufacturing issues, potentially resulting in false positives or negatives (as shown in Figure 4). The robustness of flat indenters is enhanced by the use of PMMA optical fibers embedded in 3D-printed cylindrical waveguides. Despite careful arrangement and precision cutting of the optical fibers, eliminating optical coupling issues remains challenging. Additionally, flat indenters are particularly sensitive to misalignment with the MTL, especially due to potential edge contact. In comparison, spherical indenters demonstrate greater robustness against manufacturing and mounting misalignment.

In Figure 5A,B, we present results from truncated blunted-cone punches interacting perpendicularly with the MTL on a smooth, flat steel substrate under both ambient light and dark conditions. For both scenarios, the perpendicular force detection threshold is set at 30 N for DCS#1, #2, and #3, which corresponds to ≈10 N per DCS (Figure SI5(2), Supporting Information). While DCS#1 and #2 reliably detect mechanochromic activation at 10 and 20 N, these measurements may lead to misleading conclusions about relative positioning. Indeed, similar to the flat indenters, the PMMA-based waveguide used for light reflection between mechanochromic spots and the DCS may contribute to false positives and negatives. In Figure 5C, at a 10° tilting angle under ambient light, two DCS show reliable

Flat punch on SP-PDMS thin layer on a steel substrate

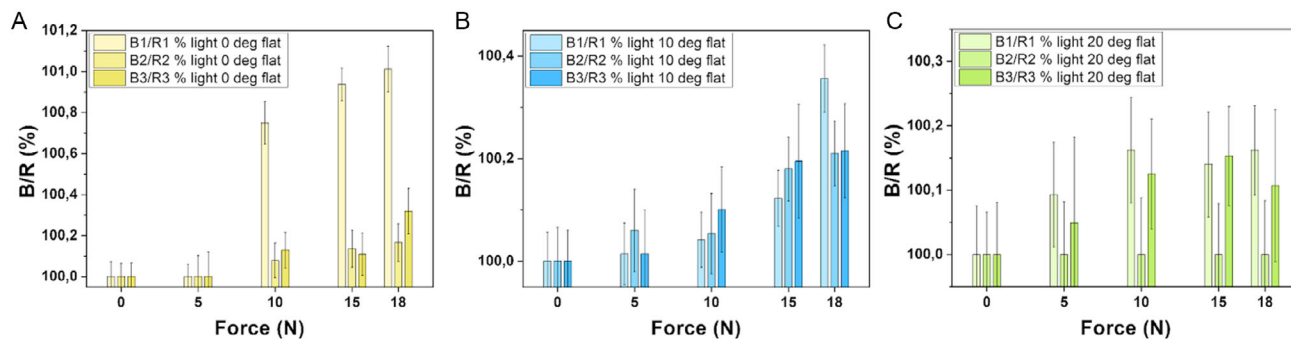


Figure 4. Experimental characterization of three flat punches on a thin SP-PDMS layer placed on a steel substrate. The variable conditions include the tilting angle between the punch shapes and the mechanochromic sample, while light conditions are kept constant. Data are presented with standard deviations, and bar values for each compression force represent the average percentage variation in the blue-to-red component from three acquisitions per channel. A) Indentation at 0° under ambient light: pale yellow indicates indenter #1, yellow denotes indenter #2, and dark yellow represents indenter #3. Hereinafter, all results labeled as indenters #1, #2, and #3 correspond to the respective DCS. The interaction is classified as nonperpendicular at an overall compression force of 18 N based on the inclination criterion. The sensory feedback does not align with the physical experiment, and the relative color detection variation between DCS #1, #2, and #3 exceeds 0.4%, indicating nonhomogeneous results. B) Indentation at 10° under ambient light: pale blue corresponds to indenter #1, blue to indenter #2, and dark blue to indenter #3. The detection system reports an overall perpendicular and homogeneous force threshold at 15 N; however, this results in false detection. C) Indentation at 20° under ambient light: pale green represents indenter #1, green for indenter #2, and dark green for indenter #3. The overall mechanochromic force detection occurs at 18 N, with color change observed only with indenter #1 (at 6 N). The lack of color detection from indenter #2 and the highly variable feedback from indenter #3 suggest a physical interaction with inclined surfaces.

Blunted cone punch on SP-PDMS thin layer on a steel substrate

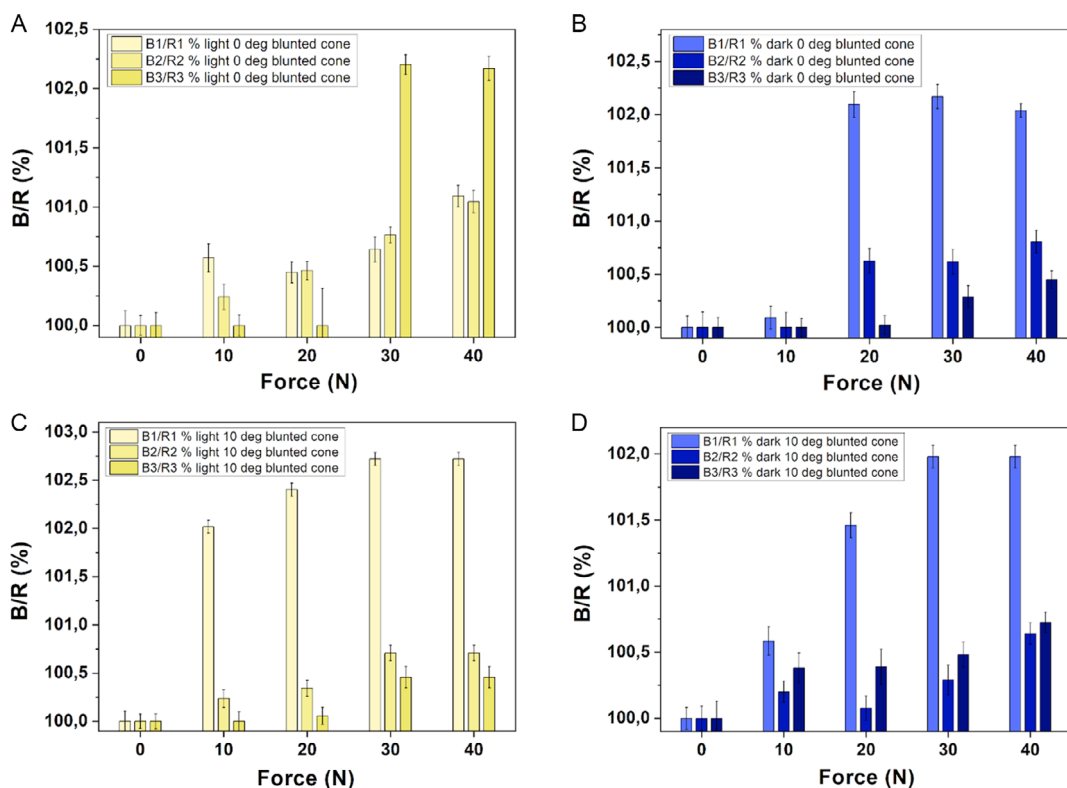


Figure 5. Experimental characterization of three blunted cone punches on a thin SP-PDMS layer placed on a steel substrate. Variables include the tilting angle and lighting conditions. Data are presented with standard deviations, and the bar values for each compression force represent the average percentage variation in the blue-to-red component from three acquisitions per channel. A) Indentation at 0° under ambient light. Pale yellow represents indenter #1, yellow corresponds to indenter #2, and dark yellow indicates indenter #3. The data labeled as indenters #1, #2, and #3 correspond to the respective DCS. A perpendicular interaction is detected with an overall mechanochromic force threshold of 30 N. However, color-changing detection is not homogeneous, potentially leading to misleading results at a force threshold of 10 N. At this threshold, DCS#1 and DCS#2 detect a color change, while DCS#3 does not, suggesting an interaction with an inclined surface and indicating a need to improve the system's robustness in detecting relative positioning. B) Indentation at 0° under dark conditions. Pale blue relates to #1 indenter, blue is for #2, and dark blue for #3. A perpendicular interaction is detected with an overall mechanochromic force threshold of 30 N, but it is not homogeneous. At a force threshold of 20 N, the feedback may suggest an interaction with an inclined surface, leading to potentially false relative positioning information. C) Indentation at 10° under ambient light. Pale yellow is related to the #1 indenter, yellow is for the #2, dark yellow is for the #3 indenter. Indenters #1 and #2 detect the force threshold at 10 N. Although the signals are not homogeneous, they indicate a physically consistent interaction with an inclined surface. At an overall compression force of 30 N, the results show that indenter #3 contacts the tilted MTL, triggering the mechanochromic effect and confirming a perpendicular condition. D) Indentation at 10° under dark conditions. Pale blue represents indenter #1, blue denotes indenter #2, and dark blue indicates indenter #3. At 10 N, the system detects mechanochromism, activating all three spots. This provides reliable information about force-threshold detection, although the relative positioning may still be misleading.

force detection at overall 10 N (i.e., around 3 N per DCS), suggesting interaction with an inclined surface and providing consistent results regarding the relative positioning of the indenters with respect to the counter-surface (Figure S15(2), Supporting Information). However, under dark conditions at the same tilting angle, all three DCS show homogeneous detection with a FC greater than 50% at overall 10 N, indicating a perpendicular condition and suggesting no inclination (Figure 5D). This result is inconsistent with the actual relative positioning of the indenters relative to the counter-surface.

As seen with flat indenters, truncated blunted-cone indenters may not offer reliable relative positioning detection but show robust performance in force-threshold detection. Additionally, these indenters show a higher percentage variation in the blue-to-red component, indicating increased sensitivity, albeit

with a wider range of compression force considered. This is likely due to the larger base of the conical shape, which acts as a waveguide with a higher numerical aperture and larger window size compared to spherical and flat shapes, allowing for greater light reflection and acquisition by the DCSs.

In conclusion, Table 1 summarizes the experimental results, and outcomes for all punch shapes under varying boundary conditions according to established reliability and robustness criteria.

2.3. Numerical Model for Pressure Distribution in MTL Lying on Half-Space Elastic System

We employ and slightly modify a semianalytical code, originally developed by Constantinescu et al.^[63] (Wolfram Mathematica), to

Table 1. Summary of the main sensory feedback outputs.

Type of indenter ^{a)}	Channel	Experimental conditions	Force threshold [N]	$P(Z > z) = 1 - P(Z \leq z) = 1 - \Phi(z)$ [%]	Force-threshold confidence parameter (if $P(Z > z) > 30\%$, then reliable force detection)	Inclination confidence parameter (if $10\% < P(Z > z) < 30\%$, then inclined surface)	
Spherical	#1	Light and 0° tilting angle	10	94.4	Local stress detection of around 3 N	Flat surface	
	#2	Light and 0° tilting angle	10	31.6	Local stress detection of around 3 N	Flat surface	
	#3	Light and 0° tilting angle	10	73.9	Local stress detection of around 3 N	Flat surface	
	#1	Dark and 0° tilting angle	16	91.8	Local stress detection of around 5 N	Flat surface	
	#2	Dark and 0° tilting angle	16	90.8	Local stress detection of around 5 N	Flat surface	
	#3	Dark and 0° tilting angle	16	48.4	Local stress detection of around 5 N	Flat surface	
	#1	Light and 10° tilting angle	10	56.7	Local stress detection of around 3 N	Flat surface	
	#2	Light and 10° tilting angle	10	74.9	Local stress detection of around 3 N	Flat surface	
	#3	Light and 10° tilting angle	10	10.2		Inclined surface	
	#1	Light and 20° tilting angle	13	72.9	Local stress detection of around 4 N	Flat surface	
	#2	Light and 20° tilting angle	13	0.0		No detection	
	#3	Light and 20° tilting angle	13	50.8	Local stress detection of around 4 N	Flat surface	
	#1	Light and 30° tilting angle	16	84.8	Local stress detection of around 5 N	Flat surface	
	#2	Light and 30° tilting angle	16	0.0		No detection	
	#3	Light and 30° tilting angle	16	82.4	Local stress detection of around 5 N	Flat surface	
	Flat	#1	Light and 0° tilting angle	18	100.0	Local stress detection of around 6 N	Flat surface
		#2	Light and 0° tilting angle	18	22.1		Inclined surface
		#3	Light and 0° tilting angle	18	34.8	Local stress detection of around 6 N	Flat surface
#1		Light and 10° tilting angle	15	42.9	Local stress detection of around 5 N	Flat surface	
#2		Light and 10° tilting angle	15	56.7	Local stress detection of around 5 N	Flat surface	
#3		Light and 10° tilting angle	15	32.3	Local stress detection of around 5 N	Flat surface	
#1		Light and 20° tilting angle	18	46.0	Local stress detection of around 6 N	Flat surface	
#2		Light and 20° tilting angle	18	3.4		No detection	
#3		Light and 20° tilting angle	18	19.8		Inclined surface	
Blunted cone	#1	Light and 0° tilting angle	30	94.8	Local stress detection of around 10 N	Flat surface	
	#2	Light and 0° tilting angle	30	100.0	Local stress detection of around 10 N	Flat surface	
	#3	Light and 0° tilting angle	30	100.0	Local stress detection of around 10 N	Flat surface	
	#1	Dark and 0° tilting angle	30	100.0	Local stress detection of around 10 N	Flat surface	
	#2	Dark and 0° tilting angle	30	79.4	Local stress detection of around 10 N	Flat surface	
	#3	Dark and 0° tilting angle	30	55.2	Local stress detection of around 10 N	Flat surface	
	#1	Light and 10° tilting angle	10	100.0	Local stress detection of around 3 N	Flat surface	
	#2	Light and 10° tilting angle	10	54.0	Local stress detection of around 3 N	Flat surface	
	#3	Light and 10° tilting angle	10	3.8		No detection	
	#1	Dark and 10° tilting angle	10	98.0	Local stress detection of around 3 N	Flat surface	
	#2	Dark and 10° tilting angle	10	50.4	Local stress detection of around 3 N	Flat surface	
	#3	Dark and 10° tilting angle	10	66.6	Local stress detection of around 3 N	Flat surface	

^{a)}For each channel of the DCS and respectively shape-dependent indenter acting on the MTL are reported the relevant outcomes as the force threshold required to trigger the mechanochromism and correlate the local stress exerted, and the relative position of the indenter with respect to the substrate. Each output is tabulated reporting the environmental and experimental conditions. Referring to the Experimental Section, the reader can derive the statistical approach to define the FC (force-threshold confidence) and IC (inclination confidence) parameters. Those parameters refer to the probability of the complement of the CDF of the standard normal distribution $\Phi(z)$, as defined in the Experimental Section. The confidence parameters are assumed reliable following the criteria defined in the main text. The local stress detection is considered as a third of the overall compression force exerted during the optomechanical characterization at which the FC satisfies the criterion. Information about perpendicularity, inclination, or no detection are extrapolated by the IC parameter. No detection means that following the criteria defined, the signal is not reliable or not detected due to no contact. Perpendicularity or inclination is referred to the relative position of the indenter respect with the substrate during contact.

determine the average contact pressure and pressure distribution of axis-symmetric, rigid, and frictionless indenters normally compressing a multilayered elastic half-space. This enables us to determine the average contact pressure on the MTL by the indenter shape and estimate the pressure distribution during compression (only shown for spherical punch form).

While experimental detection cannot capture the geometric dependency of the color-changing area during contact, the theoretical model offers insights for further investigations and design. However, the sensor's ability to confidently detect color changes is related to the punch shapes.

Considering the case of half-space contact, a spherical indenter provides an elliptical pressure distribution, which falls to zero at the contact edges and reaches its maximum at the contact center. In contrast, a sharp conical punch produces theoretically infinite stress at the tip, mitigated only by the presence of tip rounding. Finally, a flat punch generates a pressure distribution that is minimal in the center of the contact area and exhibits a square root singularity at the contact edges.^[64]

Hence, we employ an analytical-numerical algorithm to determine the average pressure at the interface, accounting for the presence of the layered system. This approach allows us to understand the influence of different punch geometries on the mechanochromic response of the SP-PDMS thin layer and serves as a

baseline for system reverse-engineering, validating experimental data, and informing MSC design. No further analytical investigations are conducted to simulate tilted interactions. The numerical model consists of the MTL perfectly bonded on an elastic half-space made of steel (Figure 6A). Both the layer and the half-space are assumed to possess homogeneous, linear, and isotropic elastic behavior.^[64,65] Additional details regarding the methodology can be found in Experimental Section. To accurately represent the system, we set Young's modulus (E) and Poisson's ratio (ν) for both the steel half-space and the MTL. The mechanical properties of the steel half-space are well-established ($E_{\text{steel}} = 210 \text{ GPa}$, $\nu_{\text{steel}} = 0.3$). To define the mechanical properties of the SP-PDMS thin layer, we conduct nanoindentation tests in a quasi-static regime (1 Hz) using a flat punch nanoindenter. The results are detailed in Figure S17, Supporting Information, and data acquisition procedures are described in Experimental Section. We investigate the mechanical properties of the MTL, as soft materials can display significant modulus variations across different length scales compared to bulkier materials (spanning three orders of magnitude^[66,67]). Young's modulus of $\approx 400 \mu\text{m}$ thick of SP-PDMS (2.5:1, 2%wt) is $E_{\text{SP-PDMS}} = 0.64 \pm 0.12 \text{ MPa}$ (Figure S17, Supporting Information). Therefore, in the numerical analyses, we consider $E_{\text{SP-PDMS}} = 0.64 \text{ MPa}$ and $\nu_{\text{SP-PDMS}} = 0.5$ as input parameters for

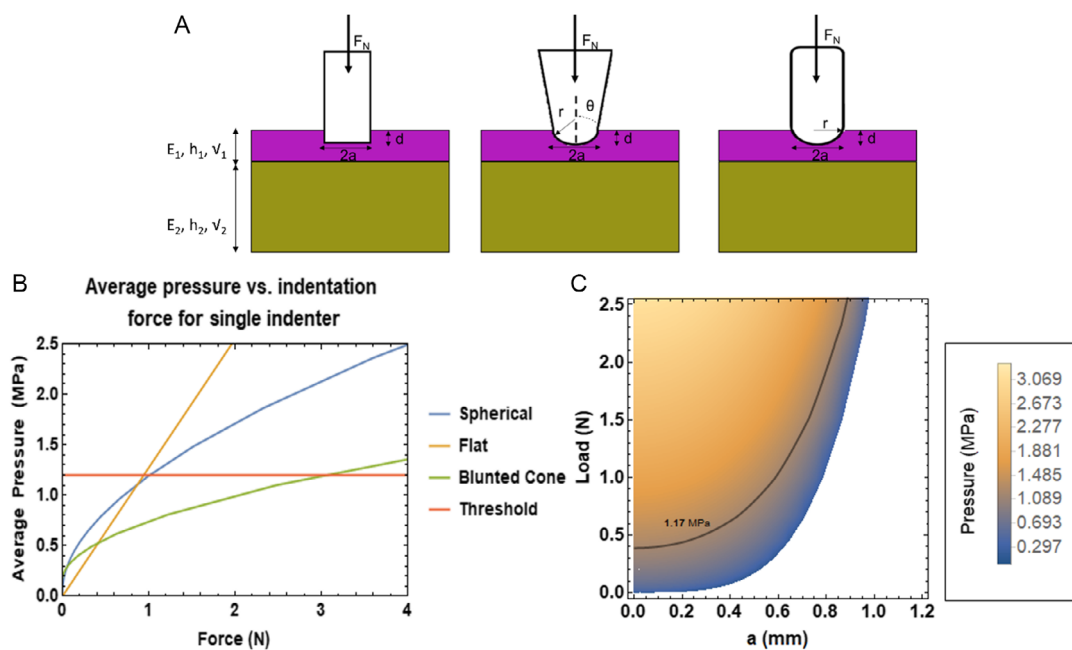


Figure 6. A) A representation of shape-variable indenters acting on a bilayered system (from left to right respectively: flat, blunted cone, and spherical indenter). In violet, it is reported the MTL, while in dark yellow the half-space of steel. Main parameters for both layers are identified as elastic modulus (E), thickness (h), and Poisson's ratio (ν). The model replicates a 1D load (F_N) acting perpendicularly on the bonded bilayer. The compression depth is identified with d , while the contact radius is identified with a . The radius of the spherical punch and of the spherical part of the blunted cone is reported with the r character. For the blunted cone also the cone-half angle is reported (θ). B) Average pressure (MPa) versus normal load applied (N) on a bilayered bonded system. Blue, orange, and green lines, respectively, represent the profile numerically generated for a spherical, flat, and blunted cone during a normal 1D indentation. The constant red line is the experimentally reported mechanochromic activation pressure (i.e., 1.17 MPa) for a bulky SP-PDMS layer as reported by Giordano et al.^[62] Thus, flat and spherical indenters with the same radius/contact radius (i.e., 0.5 mm) report the mechanochromic triggering at around 1 N, while the blunted cone ($r = 0.5 \text{ mm}$ and $\theta = 20^\circ$) generates color-changing at around 3 N. C) A 2D color map of the pressure distribution of a spherical punch compressing one-dimensionally (i.e., normally) the bilayer (MTL and steel-made half space). The color legend (right) represents how the pressure changes varying the load exerted and the contact radius of a generic spherical punch. In our case of study, the punch is rigid and it has a radius of 0.5 mm, thus generating the mechanochromic activation pressure (contour line in black) at around 0.8 N (see also panel B).

the MTL. It is noteworthy that although the steel half-space may be considered rigid relative to the soft SP-PDMS layer, we prefer to maintain a general solution method to allow for future analysis of contact conditions in more complex multilayered scenarios. The thickness of MTL is set like the experimentally adopted ($h_1 = 0.65$ mm), as well as the radii of the spherical punch ($r = 0.5$ mm), the flat punch (contact radius $a = 0.5$ mm), and the blunted cone ($r = 0.5$ mm and cone-half angle $\theta = 20^\circ$). In Figure 6B, we present the numerical results showing the average pressure profile for each shape-dependent indenter as a function of the applied normal force. The intersection of the experimental mechanochromic activation pressure threshold of 1.17 MPa^[62] with the average pressure profile determines the force threshold at which mechanochromism of the MTL is expected. The axisymmetric numerical analysis indicates that the force required to trigger the mechanochromic response for a single indenter (spherical, flat, and blunted cone) falls in the range of ≈ 1 – 3 N, which closely aligns with the experimental results for a single force-threshold detection element in the range of 3 – 10 N (Table 1). However, the numerical-derived force range for significant color change appears slightly lower than the experimental data, suggesting areas for improvement in fabrication, assembly, misalignment/optical coupling, DCS sensitivity, etc. More accurate numerical models may include the effect of interfacial adhesion due to van der Waals forces, which may have a strong effect in tiny soft contacts.^[68]

Furthermore, we present a 2D color map illustrating the pressure distribution exerted by a spherical punch on the bilayer as the contact radius (a) varies. Figure 6C provides insights into pressure distribution along the contact radius and resulting pressure on the MTL, providing a numerical representation of the chromic-activated area under different loading conditions. Numerically, we demonstrate that for a spherical punch with radius of curvature of 0.5 mm, the activation threshold is first reached at a load of about 0.4 N, while at about 0.8 N the average contact pressure reaches the threshold within a circle of radius about 0.5 mm. These findings may inspire further investigations into stimuli-responsive materials, focusing on controlling the geometric and material properties of the coupled smart layer and indenter shape to enhance local stress detection methodologies in soft contact. However, these solutions require experimental validation using optical detection systems capable of spatially resolving the color-changing area and advancements in precisely defining the mechanical properties of soft and thin materials, which remains a significant parameter in the numerical code.

2.4. Pressure Mapping in a Mechanochromic Suction Cup

Following the characterization of the MTL, we perform optomechanical experiments on the MSC (Figure 2A) to assess contact force and relative positioning during interactions with flat, curved, and sharp surfaces under both normal and angular conditions. Using the same optomechanical setup (Figure 2D) and data analysis criteria, we examine the performance of each punch shape equipped with the load-transferring/color-detection frame.

Figure 7 presents the results from at least three repetitions of mechanical compression of the MSC on a flat counter-surface (0° tilting angle) under ambient light. Figure 7A shows that spherical

punches yield a robust force detection at overall 20 N for DCS#1 and #2. Consequently, the force-sensing system detects a minimum force of ≈ 7 N per indenter during normal compression on a flat surface. However, the IC incorrectly indicates an interaction with an inclined surface, likely due to manufacturing or stacking issues within the MSC or detection system, or misalignment during contact with the multilayered soft system. This results in ambiguous information about relative positioning. The higher force threshold compared to the MTL/steel interface is likely due to the MSC's compliance, which distributes mechanical stresses over a larger contact radius. Under the same conditions, flat-ended indenters detect an overall load of 30 N but report false-negative feedback about inclined interactions (Figure 7B). Blunted cone indenters detect a robust force threshold of 40 N but provide unreliable information regarding inclination and perpendicularity (Figure 7C).

We also test the MSC's response to curved, sharp, and flat-tilted surfaces by characterizing a single spherical punch and its corresponding DCS (e.g., DCS#3) on substrates with varying shapes (Figure 8). Given the reliability issues with normal compression conditions for determining relative positioning and orientation, we focus on the interaction of a single spherical punch to test FC across different geometrical surfaces. Specifically, the MSC lies on three different PolyLactic Acid (PLA)-based 3D-printed surfaces: a curved surface with a curvature radius of 7 mm (Figure 8A,C), a cubic surface with a sharp edge (Figure 8B), and a smooth inclined plane at 30° (Figure 8D). We perform three repetitions of compression tests from 0 to 5 N for the single spherical indenter aligned with its DCS. The sensing feedback at 5 N under ambient light showed similar results for the curved surface and sharp edge (indicated by violet bars in the figure legend), suggesting that the feedback may be ineffective based on FC confidence criteria. Therefore, detecting normal interactions at the edges requires further investigation. In contrast, interactions at 45° with a curved surface and at 30° with a flat surface result in a force threshold of ≈ 5 N for the single spherical punch.

Table 2 summarizes the confidence parameters for force-threshold detection and the assessment of perpendicularity and relative positioning of the end-effector when acting perpendicular to the substrate. In conclusion, pressure mapping with the MSC—both perpendicular to a flat surface and with angular compression on variable surfaces—provides unclear information about the relative position of the end-effector. This indicates a need for further research and improvements to enhance the sensing system's ability to detect relative positioning on flat, curved, and sharp objects.

2.5. Integration of a MSC in a PneuNet Bending Actuator

Ultimately, the MSC is integrated into a PneuNet bending actuator as a proof-of-concept for the soft robotics community (Figure 9). A pneumatic tube is connected to the MSC via the casing, enabling potential suction activation upon detecting contact with an object. We qualitatively demonstrate that upon pressurization of the PneuNet, the MSC is propelled onto a flat counter-surface, initiating a color change captured by the DCS (Experimental Section). Although these findings require further

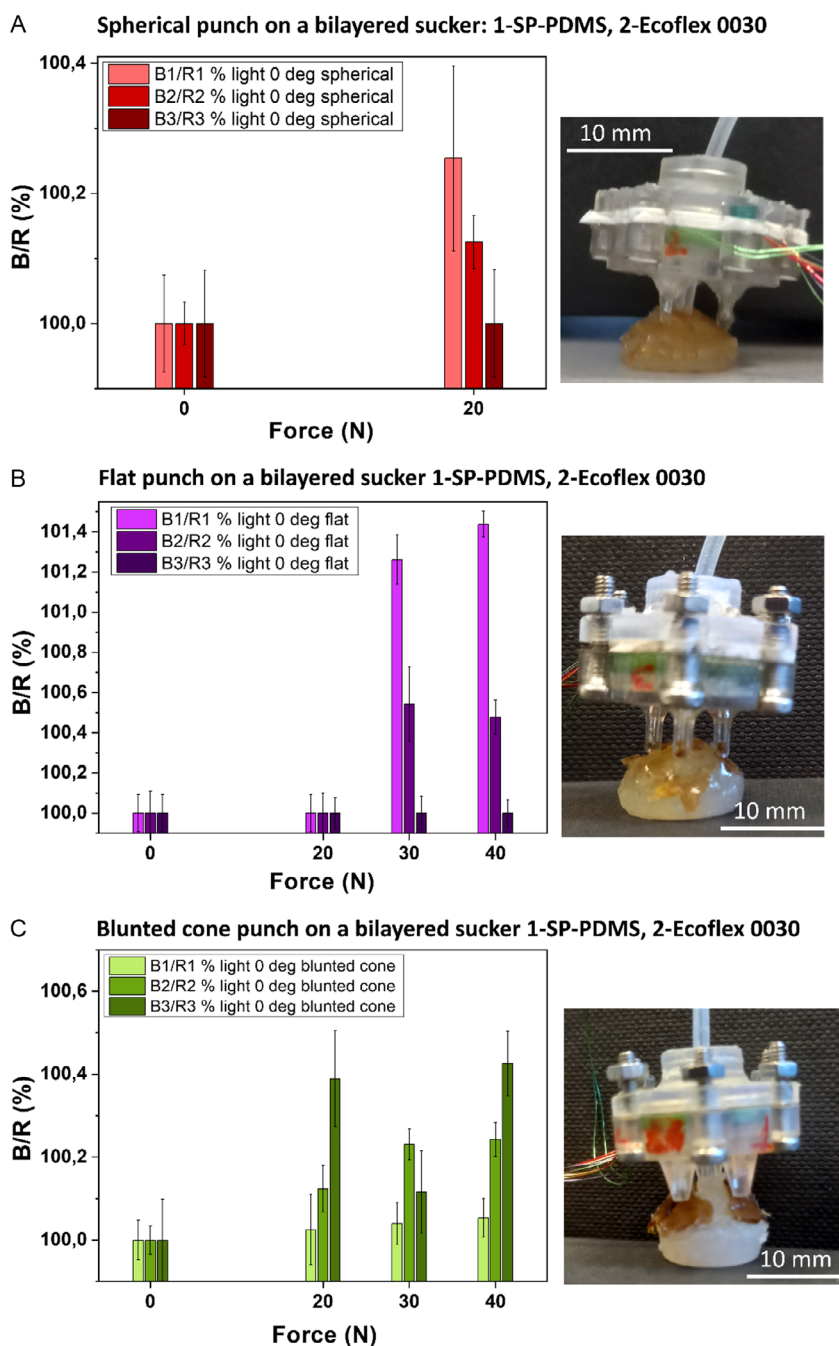


Figure 7. A) On the left, the sensory feedback output of the load-transferring and force-detection system equipped with spherical punches interacting with the MSC. The MSC consists of a bilayer structure with the MTL on top and an elastomeric Ecoflex 00-30 layer underneath in contact with the surfaces. The experimental conditions are under ambient light and at a 0° tilting angle, which are also constant for flat and blunted cone indenters. The system reliably detects color change at an overall load of 20 N for DCS#1 and #2. However, DCS#3 does not detect any change. Despite normal compression conditions, the relative positioning of the spherical indenters with respect to the counter-surface lacks physical consistency. On the right is a picture of the load-transferring and force-detection system integrated with the MSC. B) On the left, the load-transferring and force-detection system equipped with flat punches interacting with the MSC. Flat-ended indenters #1 and #2, along with their aligned DCS, can detect an overall load of 30 N, whereas DCS#3 provides no signal feedback. No reliable information about perpendicularity is obtained. On the right is a picture of the entire sensing and end-effector system. C) On the left, the blunted cone indenters interacting with the bilayered MSC. DCS#2 and #3 provide reliable force feedback at an overall compression load of 40 N. However, DCS#1's signal feedback, according to the criteria defined in the main text, may suggest inclination detection, resulting in false feedback. On the right, the picture shows the fabricated end-effector and force-detection system.

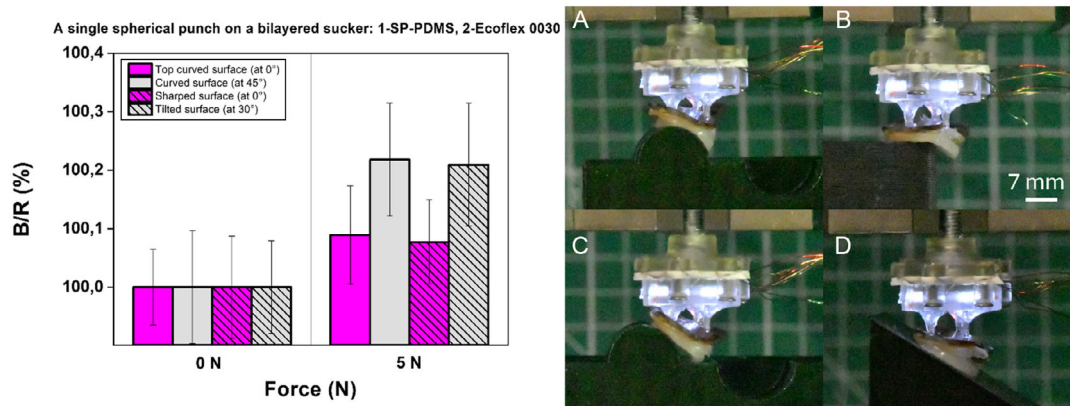


Figure 8. On the left side the sensory feedback output for a single spherical punch acting on the MSC under ambient light, with interactions on curved A,C), sharpened B), and tilted flat D) surfaces (right side). The MSC consists of a bilayer structure, with the MTL on top and an elastomeric body made of Ecoflex 00-30 at the bottom. The normalized blue-to-red percentage ratio represents the color change detection (for a single spherical punch and respective aligned DCS) at 5 N, and it is presented with error bars (see legend for interacting objects). Each experiment is repeated at least three times. The curved, sharpened, and flat surfaces are made of PLA and fabricated using an FDM printer. The curved surface has a curvature radius of 7 mm, and the tilted surface is inclined at 30°. Interaction with the curved surface is tested at the zenith (i.e., the spherical punch acting at the top of the curved surface, perpendicular to the horizontal line) in A) and at 45° in C). The color change detection is more pronounced with interaction at 45° than at the zenith position. The sharp surface is simulated using the edge of a cubic surface B), where the 5 N compression is not detected. Conversely, the tilted flat surface D) exhibits a detectable mechanochromic event, considering the discussed confidence parameters.

Table 2. Summary of the main sensory feedback outputs of the novel exteroceptive system acting on an MSC.

Type of indenter ^{a)}	Channel	Experimental conditions	Force threshold [N]	$P(Z > z) = 1 - P(Z \leq z) = 1 - \Phi(z)$ [%]	Force-threshold confidence parameter (if $P(Z > z) > 30\%$, then reliable force detection)	Inclination confidence parameter (if $10\% < P(Z > z) < 30\%$, then inclined surface)
Spherical indenter on MSC	#1	Light and 0° tilting angle	20	42.1	Local stress detection of around 7 N	Flat surface
	#2	Light and 0° tilting angle	20	61.4	Local stress detection of around 7 N	Flat surface
	#3	Light and 0° tilting angle	20	5.7		No detection
Flat indenter on MSC	#1	Light and 0° tilting angle	30	46.0	Local stress detection of around 10 N	Flat surface
	#2	Light and 0° tilting angle	30	43.6	Local stress detection of around 10 N	Flat surface
	#3	Light and 0° tilting angle	30	5.6		No detection
Blunted cone indenter on MSC	#1	Light and 0° tilting angle	40	17.6		Inclined surface
	#2	Light and 0° tilting angle	40	90.3	Local stress detection of around 13 N	Flat surface
	#3	Light and 0° tilting angle	40	86.0	Local stress detection of around 13 N	Flat surface

^{a)}For each channel of the DCS and respectively shape-dependent indenter, we report the local stress required to trigger the mechanochromism and correlate the force generated during mechanical compression (normal), and the relative position of the indenter with respect to the substrate. Each output is tabulated reporting the environmental and experimental conditions. The probability values related to the confidence parameters (i.e., FC and IC) are relatively lower in absolute terms with respect to the tabulated values characterizing the sensory feedback on the MTL. As reported in Table , the reader can refer to the Experimental Section to understand the statistical approach. The reliability and robustness of the entire system in terms of force detection and relative position follow the criteria defined in the main text.

statistically grounded data acquisition and analysis, they showcase the capability of mechanochromically based exteroceptive sensing systems to detect forces generated by pneumatic actuators. Additionally, we emphasize that the compact dimensions of the sensor system allow seamless integration into actuators without compromising overall performance. However, we observe

that integration requires improvement. Upon pressurization, the bending motion of the PneuNet cannot be precisely controlled, causing the MSC to be slightly inclined relative to the counter-surface. This inclination makes it difficult to determine information about the perpendicularity and relative position of the end-effector.

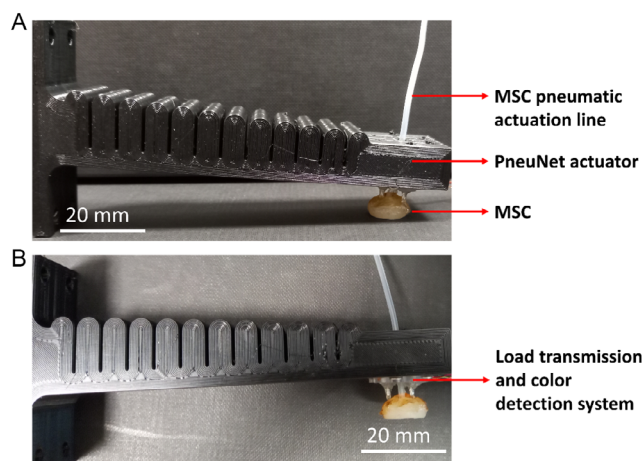


Figure 9. a) Side views of the PneuNet proof-of-concept endowed with the MSC, b) and the load transmission and color detection system.

3. Conclusion

We present an innovative methodology for detecting local contact stresses within a soft manipulative end-effector, coupled with the simultaneous determination of its spatial orientation relative to the interacting object. This is accomplished by leveraging mechanochromism, which correlates color alterations with compression loads induced by actuation. Experimental validations demonstrate the effectiveness of three distinct solutions acting as force-threshold detection systems, capable of assessing different degrees of interaction between the soft end-effector and a rigid substrate. Additionally, we introduce statistical parameters to ensure the robustness and reliability of the entire sensing system under varying environmental conditions.

This study demonstrates the possibility of customizing activation force, applicable both to MTL and MSC, according to the specific requirements of different end-effectors. This customization involves adjusting parameters such as indenter diameter, shape, constitutive materials, and quantity, as well as modifying the actuation mechanism. Numerical solutions are employed to investigate these parameters, providing theoretical insights for reverse-engineering or enhancement purposes. However, the mechanochromic activation force is constrained by the local high-stress threshold required to initiate color change in the mechanochromic material formulation. Developing mechanochromic materials with lower activation stresses would enable piezochromic exteroceptive sensing elements for applications involving forces below 10 N (≈ 3 N per indenter as demonstrated in this study). The potential of multipoint detection to anticipate contact angle and position of the MTL and/or suction cup relative to the mechanical interaction surface is evident. While this study primarily focuses on discerning and quantifying perpendicular or inclined contact between the MSC and object, future work could involve signal triangulation considering three detection points on the MSC and potentially across three MSCs distributed along an entire manipulative end-effector. This approach, combined with intensity-based data analyses from the three DCS (or via spectroscopic acquisition with miniaturized photonic

assemblies), could accurately predict contact angle, position, and even the degree of contact, especially with objects exhibiting variable asperities and/or stiffness.

Nevertheless, this study highlights the need for further improvements in optical coupling detection, particularly for detecting mechanical interactions and determining the end-effector's relative position on inclined, sharp, or highly curved surfaces, as evidenced by the MSC characterization results. The sensitivity of color detection is closely linked to the waveguide design, impacting the reflected light cone and window size of the color detection devices. Design parameters, construction techniques, and material choices may influence system reliability and require thorough design considerations for various application scenarios. Despite existing limitations, they do not significantly compromise the effectiveness of the force-detection solution.

Moreover, further exploration is warranted for real-time, object-independent, closed-loop, and teleoperated grasping methods that incorporate our solution. In our envisioned scenario, a pneumatically driven three-fingered robotic system equipped with MSCs, along with the load transfer and color detection system, approaches an object, detects the exerted force, and provides force-feedback on the operator's screen, accompanied by a confidence percentage value indicating relative position. This serves as a reference for force-threshold/relative position data, enabling the operator to adjust the actuation module for suction procedures and multifaceted grasping strategies. Additional information may be presented in teleoperation videos, facilitating end-effector orientation estimation in 3D space. The integration of machine learning techniques and supervised algorithms may be necessary to collect deducible information and enhance the dexterity of the robotic system.^[69]

Case studies that could benefit from this type of solution, include robotic manipulators and grippers for precision and safe crop harvesting,^[70] actuators designed to address ocean pollution,^[54,71] and systems for close and respectful exploration of underwater life.^[72] Additionally, wearables or minimally invasive surgical tools for safe and precise medical applications^[62,73] stand to gain from this technology. Furthermore, this solution may enhance haptic human-machine interfaces that require precise force and local stress detection as in precision mechanical industries and collaborative robotics.^[55,74,75] In conclusion, our proposed system could significantly expand the capabilities of soft robotics by enhancing the exteroceptive information available to manipulators. This could benefit industries and workers operating in challenging environments through the integration of advanced autonomous technologies. This study may represent a crucial step forward in developing intelligent, mechanically responsive sensors for object retrieval across diverse environments.

4. Experimental Section

Fabrication of the SP-PDMS Thin Layer: MTL is fabricated by covalently crosslinking the bisalkene-terminated SP molecule^[76,77] and the PDMS (Sylgard 184) network (Figure S15(1), Supporting Information). The synthesis and characterization of SP are reported elsewhere.^[62] All the reagents are purchased from Sigma-Aldrich and used without further purification. To prepare the thin layers, 2% wt bifunctionalized SP molecule is

dissolved in DCM (Sigma Aldrich) in a 5 mL glass vial with 2.5:1 prepolymer/curing agent ratio of PDMS (w/w). The mixture is stirred for 1 h. Separately, a solution of sucrose with a concentration of 30% in water is prepared and stirred. The 50 mL solution is then poured onto a thin aluminum foil and baked in an oven at $\approx 90^\circ\text{C}$ until the excess of water is removed completely (around 1 h). This process results in a highly hydrated sacrificial thin layer of sugar that coats the aluminum foil. In a glass vacuum chamber, we gently allow to evaporate a few milliliters of DCM dissolving the SP-PDMS mixture. The SP-PDMS mixture is then poured homogeneously onto the sucrose-coated aluminum foil placed on a flat, level surface, ensuring a uniform distribution (Figure S18, Supporting Information). A level is used to ensure that the surface is perfectly horizontal, and the solution is manually spread to achieve an even layer. The large MTL (20×20 mm) is cured in an oven at around 90°C for 3 h. After removing it from the oven, a few drops of water are applied to wet the border of the aluminum foil, facilitating the delamination of the MTL, which now appears in a dark-orange coloration. Its averaged thickness is 0.65 ± 0.08 mm and it is measured using an electronic digital caliper. The thin layer is manually cut with a blade and bonded to the elastomeric body of the suction cup by thermal curing at 90°C for 3 h (Figure S18, Supporting Information).

Fabrication of the Suction Cups and Color Detection System: The suction cups are fabricated using the cast molding technique. We utilize a set of 3D-printed molds specifically designed for open suction cups, as described in Mazzolai et al.^[74] The molds utilized are produced using an SLA printer (Formlabs 2) and are comprised of two parts, incorporating a concentric hollow tubular insert designed to accommodate the pneumatic silicone tube. The initial mold (Mold A in Figure S18, Supporting Information) is employed for fabricating the dome-like body of the suction cup, with an average thickness of 3.5 ± 0.3 mm and a diameter of 11.00 ± 0.01 mm. Minor thickness variations may occur due to mechanical clamping of the upper portion of the mold during the precured elastomeric liquid phase. Notably, thermal expansion influences the resulting thickness during the curing process at 90°C for ≈ 1 h.

A secondary mold (Mold B in Figure S18, Supporting Information) is employed to cast the SP-doped PDMS thin layer on top of the suction cup. Mold B is treated with Polytetrafluoroethylene spray on its internal part to facilitate easy release of the silicone and improve surface homogeneity (Figure S18, Supporting Information). This mold houses the thin SP-doped PDMS layer, with a thickness of 0.65 ± 0.08 mm, facilitating the coating of the suction cups. The bonding process involves placing the MTL on top of the Ecoflex00-30 body and subjecting it to thermal curing at 90°C for 3 h. Prior to MTL placement, a few drops of Ecoflex00-30 are applied to the surface to enhance bonding, albeit potentially introducing some inhomogeneities. The top part of Mold B is then pressed with bolts and screws to prevent thermal expansion during curing, ensuring consistent film quality. Concurrently, this process serves to affix the pneumatic tube to the suction cup body. The tube, featuring an internal diameter of 0.8 mm, serves as a stalk and traverses along the housing frame for the color detection system. The tube is separately connected to a dedicated fluidic line, employed for generating adhesion when the sensing system provides force-detection feedback.

The top and bottom part of the load-transferring and color detection system casing are fabricated with an SLA printer (Formlabs 2) in Clear Resin (FormLabs, $E = 2.6$ GPa) with a resolution of $25\ \mu\text{m}$. After the printing process, the parts are washed in isopropanol for 10 min and then cured for 30 min at 60°C with a UV-LED ($405\ \text{nm}$ – $1.25\ \text{mW cm}^{-2}$). The design of the casing is reported in Figure S13, Supporting Information (maximum external diameter 22.3 mm, maximum height 16.8 mm). The design is custom made to accommodate the PCB (diameter 13.60 mm, thickness 1.54 mm), whose schematic is reported in Figure S16, Supporting Information. The rounded PCB consists of three DCS (VEML6040, Vishay Semiconductors) in close arrangement with respective three white LED (LTW-C191T55, Lite-On) controlled by an ARM-microcontroller unit (CY8C4014LQI-421QFN, Infineon Technologies). The DCS senses red, green, and blue components (RGB) and embeds an analog-to-digital converter to convert current intensity associated to each color to digital values. The integration time is set to 40 ms (25 Hz

acquisition frequency). To maximize performances, the window size of each DCS should be large enough to optimize the retro-reflected light irradiating the sensor. By construction, the center of each DCS and the center of the window, that in our case is the center of the waveguide acting also as indenter, are aligned. However, for construction constraint, the window size is small (maximum mechanochromic area is $0.785\ \text{mm}^2$) and the waveguide length is 5 ± 0.5 mm (i.e., distance from the DCS and the indented area) to perfectly transfer the load with the indenters' tips. In this condition the relative sensitivity of the VEML6040 reported in the data-sheet is low (i.e., 10–20%). To achieve a higher relative sensitivity waveguide parameter, distances, and the window size should be optimized considering the applicative constraints. Due to the low VEML6040 sensitivity in this specific arrangement, we maximize the optical collection of the retro-illuminated color-changing spot size, adjusting the forward driving current ($\approx 201.7\ \mu\text{A}$) using a variable resistor (1 k Ω), and adopting bare PMMA optical fibers or few drops of microscope oil (Immorsol 518F, Carl Zeiss) in the tubular indenters' structure. The data acquired and converted from the DCS are driven to the ARM-microcontroller unit. The latter is a combination of a microcontroller with standard communication and timing peripherals required to synchronize the color detection and light source system. The DCS board is connected to a data acquisition module powered with a 3.7 V rechargeable lithium battery. Data are then transferred by Bluetooth directly to the control read-out and acquisition system connected to a PC by USB. A custom-made software with a user-friendly GUI (developed in Visual Studio 2017) acquires, visualizes, and records real-time the RGB components of each DCS and the white light at 10 Hz.

Optomechanical Setup: The custom optomechanical setup is engineered utilizing the UTM (Zwick/Roell 2005) as a linear trail for compression force measurements. The housing frame is securely clamped to a 50 N force cell (Zwick/Roell Xforce P), serving dual functions: as an indentation element and as a color change detector, thus facilitating both the detection of force and the analysis of geometrically variable punch indentations.

During MTL characterization, the sample is positioned on a thick steel substrate. For angular characterization, a goniometric manual stage (Newport) is employed to tilt the thin layer. Measurements conducted under ambient light conditions consistently occur within the same room, maintaining consistent environmental illumination. Dark condition simulations involve conducting measurements during sunlight and covering the entire UTM with a large black box for professional photographers.

The experimental protocol entails the gradual approach of the 3D-printed frame to the sample at a rate of $0.5\ \text{mm min}^{-1}$ until the load cell registers a few decimal points of Newton force, indicating a steady-state position at 0 N. At this point, the DCS setup initiates recording of all RGB components for the three-color sensors. Subsequently, a predetermined series of compression force thresholds is established for each experiment. For instance, when employing spherical punches on the MTL atop a steel substrate at a 0° angle under ambient light, the force set configuration comprises 0, 5, 10, 13, and 16 N thresholds. The UTM is programmed to reach the 5 N threshold at a velocity of $20\ \text{mm min}^{-1}$, followed by a 2 s pause to allow the elastomeric layer to relax after mechanical perturbation. Subsequently, the linear trail retracts at $12\ \text{mm min}^{-1}$ to return to the 0 N steady-state condition, with software facilitating positional control. It remains in this position for 50 s to assess potential color changes and allow for recovery from color fading. This process is repeated for compression tests at 10 N ($20\ \text{mm min}^{-1}$ velocity, 2 s pause, and 50 s rest) and continues incrementally until reaching the maximum pre-set force threshold.

In this way, the temporal automated system allowed the optical signal integration after the compression and the elastomeric relaxation time-phase (a steady-state customized protocol). The maximum compression force threshold considered is 40 N for the truncated blunted cone.

Nanoindentation Tests: The SP-PDMS thin layers in different prepolymer/curing agent ratio (2.5:1, 5:1, 10:1, 15:1) and different %wt of SP covalently bonded (1%, 2%, 4%, 5%) are tested with the Nanoindenter (KLA Instruments iNano) in a perpendicular configuration, with the method of dynamic flat punch complex modulus. The tip adopted is a cylindrical flat punch with a diameter of $109\ \mu\text{m}$. We test them in a quasi-static regime at

1 Hz, without analyzing viscoelastic properties and acquiring the storage modulus (i.e., Young's modulus). For each test, from 3 to 7 points are acquired and we repeat the test at least three times. The averaged data and error bars are reported in Figure S17, Supporting Information. Comparing Figure S12–S17, Supporting Information, it is worth noting that there is a significant difference, approximately one order of magnitude, between Young's modulus obtained from nanoindentation tests on a thin layer and conventional macroscopic tensile testing techniques.^[62]

Numerical Code: For exhaustive documentation about the code (Wolfram Mathematica), we refer the reader to literature.^[63,65] We report the crucial information and the modifications we apply. We limit our analysis to perfectly bonded sublayers, considering a frictionless interaction between rigid punch shapes and an MTL bonded to a steel-made half-space. The system operates in a 1D setting with axisymmetry, no angular dependence or shear stresses (i.e., normal indentation), and in air. We assume small deformations and rely on the validity of the half-space hypothesis ($h_2 = \infty$) applicable when the contact radius (a) is much smaller than the thickness of the substrate.

Numerical results for average pressure are defined consistently with experimental parameters (geometry, materials, thickness, etc.), yielding dimensional output. The developed code by Constantinescu et al.^[63] returns dimensionless results, i.e., which are independent from the thickness of the thin layer. For theoretical equations and algebraic correlations, readers may refer to the handbook of Popov et al.^[64]

From the code, we extract lists of loads and contact radii to establish the relationship between average pressure and load, determining the shape-dependent punch loads that trigger MTL activation threshold (i.e., 1.17 MPa). Additionally, we evaluate a 2D color map illustrating the pressure distribution exerted by a spherical punch as the contact radius varies. This entails numerical calculation of surface tractions for $r < a$ using the integral function defined by Constantinescu et al.^[63] yielding stress variation along the layer with varying contact radius and load. The modified code provides a contour plot with the x-axis representing contact radius, the y-axis representing normal load, and the color legend indicating pressure variation. All outputs are dimensional and scaled to match physical dimensions consistent with experimental data.

Statistical Analysis: The acquired data for characterizing the MTL and MSC undergo evaluation using Microsoft Office Excel 2016 and OriginPro 2022 v.9.9 from OriginLab. MTL samples are randomly obtained by manually blade-cutting larger samples obtained from delamination, ensuring statistical consistency across different regions indented for each sample (Figure S18, Supporting Information). At least three repetitions are considered for each translucent frame endowed with variable shape punches, tilting angle, and environmental condition. Each repetition involves acquiring 12 color components (3 channels RGB for 3 sensors, and 3 white components) at each time step (as set by the integration time of the DCS) following the optomechanical compression–relaxation procedure. The data are reported with the averaged value (in percentage) and the corresponding percent standard deviation.

The procedure includes normalization of all color components with respect to the white component of the respective sensor (e.g., $R_{\#1}/W_{\#1}$, $G_{\#1}/W_{\#1}$, $B_{\#1}/W_{\#1}$), calculation of the blue-to-red ratio values (e.g., $B_{\#1}/R_{\#1}$, $B_{\#2}/R_{\#2}$, $B_{\#3}/R_{\#3}$), and averaging of values during the compression and relaxation phases, with manual removal of values during slopes (i.e., following experimental compression protocol these regards relaxation timing and linear trail movements). We consider the averaged blue-to-red values for the time range in which the frame is in the steady-state condition, both at 0 N and after MTL/MSD compression. This procedure is repeated for all measurements at each force step and static time. The blue-to-red ratio values are then normalized with respect to the minimum value at 0 N (i.e., the averaged value of $B_{\#1}/R_{\#1}$, $B_{\#2}/R_{\#2}$, $B_{\#3}/R_{\#3}$ at 0 N), scaled to 100% for each acquisition, enabling consistent increase in output percentage if mechanochromism is triggered.

FC and IC parameters are evaluated comparing two normal distributions: 1) at 0 N (σ_2 , μ_2); and 2) at the compression force value (σ_1 , μ_1), for every sensor's blue-to-red ratio. This evaluation is contingent upon the requisite assumption that mechanochromism activation necessitates $\mu_1 > \mu_2$. By considering the independence of Gaussian distributions

and leveraging the properties of sums of Gaussian random variables, we establish that the essential and comprehensive prerequisite for mechanochromism activation is the constant fulfillment of $\mu_1 - \sigma_1$ being greater than $\mu_2 + \sigma_2$, under the premise that $\mu_1 > \mu_2$. Since $\mu_1 > \mu_2$, we defined a new random variable $Y = \mu_1 - \sigma_1 - (\mu_2 + \sigma_2) = X_1 - X_2$, where $X_1 \approx N(\mu_1, \sigma_1^2)$ and $X_2 \approx N(\mu_2, \sigma_2^2)$ are the two Gaussian random variables representing the distributions with means μ_1 and μ_2 , and standard deviations σ_1 and σ_2 , respectively. Thus, $\mu_Y = \mu_1 - \mu_2$ and variance $\sigma_Y^2 = \sigma_1^2 + \sigma_2^2$, defining the Gaussian distribution $Y \approx N(\mu_Y, \sigma_Y^2)$. We then calculated the probability that $Y > \sigma_1 + \sigma_2$, i.e., $P(Y > \sigma_1 + \sigma_2)$. To evaluate this probability, we can standardize Y by subtracting the mean and dividing by the standard deviation. Let $Z = (Y - \mu_Y)/\sigma_Y$, which follows a standard normal distribution, $Z \approx N(0, 1)$. Thus, $P(Z > (\sigma_1 + \sigma_2 - \mu_Y)/\sigma_Y)$ is the probability of Z being greater than a specific value $z = (\sigma_1 + \sigma_2 - \mu_Y)/\sigma_Y$. This probability can be calculated using the complement of the CDF of the standard normal distribution $\Phi(z)$: $P(Z > z) = 1 - \Phi(z)$.

All the plots are generated by Origin 2022 v.9.9.

PneuNet Fabrication and Qualitative Experiments: The PneuNet bending actuator is manufactured using a Prusa i3 MK3S+ Fused Deposition Modeling printer, employing black thermoplastic polyurethane filament with a Shore A hardness of 98 A. The actuator design is based on a variation of the design presented by Scharff et al.^[78] featuring a void in the tip to accommodate the casing of the color detection system. Since the qualitative experiment is not statistically grounded, the PneuNet is secured in a clamp to remain parallel to the base of a digital scale. When the PneuNet is inflated, the MSC is moved onto the flat counter-surface. The pressure exerted by the indenters on the MSC triggers a color change, which is captured by the DCS. The color change footprint is confirmed visually.

Supporting Information

Supporting Information is available from the Wiley Online Library or from the author.

Acknowledgements

The authors would like to thank Stein van Veggel for his visualization skills exhibited in Figure 1. Stein's input nicely illustrates the working principle of this research and makes it easier to grasp for the readers. The authors are grateful for his contribution. C.F., A.M., and B.M. are part of the RAISE Innovation Ecosystem. G.G. and A.P. were supported by the European Union (ERC-2021-STG, "Towards Future Interfaces With Tuneable Adhesion By Dynamic Excitation" - SURFACE, Project ID: 101039198, CUP: D95F22000430006). Views and opinions expressed are however those of the authors only and do not necessarily reflect those of the European Union or the European Research Council. Neither the European Union nor the granting authority can be held responsible for them. G.G. and A.P. were partly supported by the Italian Ministry of University and Research under the program "Department of Excellence" Legge 232/2016 (grant no. CUP - D93C23000100001).

Conflict of Interest

The authors declare no conflict of interest.

Author Contributions

Goffredo Giordano and **Barbara Mazzolai**: conceived the concepts. **Goffredo Giordano**: conceived and conducted the experiments and data analyses. **Rob Bernardus Nicolaas Scharff** and **Goffredo Giordano**: fabricated and designed the frames for digital color sensors and the pneumatic actuator. **Goffredo Giordano**, **Marco Carloti**, and **Mariacristina Gagliardi**: performed the chemical synthesis of the mechanochromic unit. **Goffredo**

Giordano fabricated the mechanochromic thin layer and the suction cups and assembled the setups. **Goffredo Giordano** and **Antonio Papangelo**: defined and modified the numerical code for contact analyses. **Alessio Mondini**: designed and assembled the electronics and performed experiments. **Goffredo Giordano** and **Carlo Filippeschi**: conducted nanoindentation tests. **Goffredo Giordano**: wrote the manuscript. All authors interpreted the data. All authors read, edited, and discussed the manuscript and agree with the claims made in this work. **Barbara Mazzolai**: coordinated and supervised the research.

Data Availability Statement

The data that support the findings of this study are available from the corresponding author upon reasonable request.

Keywords

contact mechanics, manipulation, mechanochromism, object interactions, piezochromic sensor, soft gripper, stress detection

Received: March 29, 2024

Revised: August 16, 2024

Published online:

- [1] H. Wang, M. Totaro, L. Beccai, *Adv. Sci.* **2018**, *5*, 1800541.
- [2] T. Bu, T. Xiao, Z. Yang, G. Liu, X. Fu, J. Nie, T. Guo, Y. Pang, J. Zhao, F. Xi, C. Zhang, Z. L. Wang, *Adv. Mater.* **2018**, *30*, 1800066.
- [3] T. G. Thuruthel, B. Shih, C. Laschi, M. T. Tolley, *Sci. Rob.* **2019**, *4*, eaav1488.
- [4] H. Niu, H. Li, S. Gao, Y. Li, X. Wei, Y. Chen, W. Yue, W. Zhou, G. Shen, *Adv. Mater.* **2022**, *34*, 2202622.
- [5] J. Shintake, V. Cacciuolo, D. Floreano, H. Shea, *Adv. Mater.* **2018**, *30*, 1707035.
- [6] W. Heng, S. Solomon, W. Gao, *Adv. Mater.* **2022**, *34*, 2107902.
- [7] C. Laschi, B. Mazzolai, M. Cianchetti, *Sci. Rob.* **2016**, *1*, eaah3690.
- [8] Z. Xia, V. D. Alphonse, D. B. Trigg, T. P. Harrigan, J. M. Paulson, Q. T. Luong, E. P. Lloyd, M. H. Barbee, S. L. Craig, *Molecules* **2019**, *24*, 542.
- [9] B. Shih, D. Shah, J. Li, T. G. Thuruthel, Y.-L. Park, F. Iida, Z. Bao, R. Kramer-Bottiglio, M. T. Tolley, *Sci. Rob.* **2020**, *5*, eaaz9239.
- [10] Z. Shen, F. Chen, X. Zhu, K.-T. Yong, G. Gu, *J. Mater. Chem. B* **2020**, *8*, 8972.
- [11] D. Yan, Z. Wang, Z. Zhang, *Acc. Chem. Res.* **2022**, *55*, 1047.
- [12] A. S. Kozlenko, I. V. Ozhogin, A. D. Pugachev, M. B. Lukyanova, I. M. El-Sewify, B. S. Lukyanov, *Top. Curr. Chem.* **2023**, *381*, 8.
- [13] C. Micheletti, V. A. Dini, M. Carloti, F. Fuso, D. Genovese, N. Zaccaroni, C. Gualandi, A. Pucci, *ACS Appl. Polym. Mater.* **2023**, *5*, 1545.
- [14] Y. Yu, J. Li, S. A. Solomon, J. Min, J. Tu, W. Guo, C. Xu, Y. Song, W. Gao, *Sci. Rob.* **2023**, *7*, eabn0495.
- [15] G. Soter, A. Conn, H. Hauser, J. Rossiter, in *2018 IEEE Int. Conf. on Robotics and Automation (ICRA)*, Brisbane, QLD, Australia **2018**, pp. 2448–2453.
- [16] C. C. Nguyen, S. Wong, M. T. Thai, T. T. Hoang, P. T. Phan, J. Davies, L. Wu, D. Tsai, H.-P. Phan, N. H. Lovell, T. N. Do, *Adv. Sens. Res.* **2023**, *2*, 2200036.
- [17] T. Kim, J. W. Lee, C. Park, K. Lee, C. E. Lee, S. Lee, Y. Kim, S. Kim, S. Jeon, D. Y. Ryu, W.-G. Koh, C. Park, *Nano Energy* **2022**, *92*, 106688.
- [18] G. R. Gossweiler, C. L. Brown, G. B. Hewage, E. Sapiro-Gheiler, W. J. Trautman, G. W. Welshofer, S. L. Craig, *ACS Appl. Mater. Interfaces* **2015**, *7*, 22431.
- [19] G. Giordano, M. Carloti, B. Mazzolai, *Adv. Mater. Technol.* **2021**, *6*, 2100437.
- [20] Z. Wang, Z. Ma, Y. Wang, Z. Xu, Y. Luo, Y. Wei, X. Jia, *Adv. Mater.* **2015**, *27*, 6469.
- [21] C. R. Hickenboth, J. S. Moore, S. R. White, N. R. Sottos, J. Baudry, S. R. Wilson, *Nature* **2007**, *446*, 423.
- [22] Z. Li, R. Toivola, F. Ding, J. Yang, P. N. Lai, T. Howie, G. Georgeson, S. H. Jang, X. Li, B. D. Flinn, A. K. Y. Jen, *Adv. Mater.* **2016**, *28*, 6592.
- [23] S. L. Potisek, D. A. Davis, N. R. Sottos, S. R. White, J. S. Moore, *J. Am. Chem. Soc.* **2007**, *129*, 13808.
- [24] C. Calvino, A. Guha, C. Weder, S. Schrettl, *Adv. Mater.* **2018**, *30*, 1704603.
- [25] D. A. Davis, A. Hamilton, J. Yang, L. D. Cremer, D. Van Gough, S. L. Potisek, M. T. Ong, P. V. Braun, T. J. Martínez, S. R. White, J. S. Moore, N. R. Sottos, *Nature* **2009**, *459*, 68.
- [26] H. Chen, F. Yang, Q. Chen, J. Zheng, *Adv. Mater.* **2017**, *29*, 1606900.
- [27] M. H. Barbee, K. Mondal, J. Z. Deng, V. Bharambe, T. V. Neumann, J. J. Adams, N. Boechler, M. D. Dickey, S. L. Craig, *ACS Appl. Mater. Interfaces* **2018**, *10*, 29918.
- [28] H. Qian, N. S. Purwanto, D. G. Ivanoff, A. J. Halmes, N. R. Sottos, J. S. Moore, *Chem* **2021**, *7*, 1080.
- [29] C. Li, Q. He, Y. Wang, Z. Wang, Z. Wang, R. Annapooranan, M. I. Latz, S. Cai, *Nat. Commun.* **2022**, *13*, 3914.
- [30] H. Yuk, S. Lin, C. Ma, M. Takaffoli, N. X. Fang, X. Zhao, *Nat. Commun.* **2017**, *8*, 14230.
- [31] Q. Wang, G. R. Gossweiler, S. L. Craig, X. Zhao, *Nat. Commun.* **2014**, *5*, 13433.
- [32] S. A. Morin, R. F. Shepherd, S. W. Kwok, A. A. Stokes, A. Nemiroski, G. M. Whitesides, *Science* **2012**, *337*, 828.
- [33] C. Xu, M. Colorado Escobar, A. A. Gorodetsky, *Adv. Mater.* **2020**, *32*, 1905717.
- [34] H. H. Chou, A. Nguyen, A. Chortos, J. W. F. To, C. Lu, J. Mei, T. Kurosawa, W. G. Bae, J. B. H. Tok, Z. Bao, *Nat. Commun.* **2015**, *6*, 8011.
- [35] J. H. Pikul, S. Li, H. Bai, R. T. Hanlon, I. Cohen, R. F. Shepherd, *Science* **2017**, *358*, 210.
- [36] J. Park, Y. Lee, M. H. Barbee, S. Cho, S. Cho, R. Shanker, J. Kim, J. Myoung, M. P. Kim, C. Baig, S. L. Craig, H. Ko, *Adv. Mater.* **2019**, *31*, 1808148.
- [37] R. T. Hanlon, J. B. Messenger, in *Cephalopod Behaviour*, Cambridge University Press, Cambridge, England **2018**.
- [38] A. McDougal, B. Miller, M. Singh, M. Kolle, *J. Opt.* **2019**, *21*, 073001.
- [39] S. van Veggel, M. Wiertlewski, E. L. Doubrovski, A. Kooijman, E. Shahabi, B. Mazzolai, R. B. N. Scharff, *Adv. Sci.* **2024**, *11*, 2400806.
- [40] B. Di Credico, G. Griffini, M. Levi, S. Turri, *ACS Appl. Mater. Interfaces* **2013**, *5*, 6628.
- [41] Y. Li, Z. Ma, A. Li, W. Xu, Y. Wang, H. Jiang, K. Wang, Y. Zhao, X. Jia, *ACS Appl. Mater. Interfaces* **2017**, *9*, 8910.
- [42] P. Gumbley, S. W. Thomas, *ACS Appl. Mater. Interfaces* **2014**, *6*, 8754.
- [43] W. Deng, Y. Zhou, A. Libanori, G. Chen, W. Yang, J. Chen, *Chem. Soc. Rev.* **2022**, *51*, 3380.
- [44] M. Qin, M. Sun, R. Bai, Y. Mao, X. Qian, D. Sikka, Y. Zhao, H. J. Qi, Z. Suo, X. He, *Adv. Mater.* **2018**, *30*, 1800468.
- [45] M. Ding, L. Jing, H. Yang, C. E. Machnicki, X. Fu, K. Li, I. Y. Wong, P.-Y. Chen, *Mater. Today Adv.* **2020**, *8*, 100088.
- [46] M. Vatankeh-Varnosfaderani, A. N. Keith, Y. Cong, H. Liang, M. Rosenthal, M. Sztucki, C. Clair, S. Magonov, D. A. Ivanov, A. V. Dobrynin, *Science* **2018**, *359*, 1509.
- [47] T. Q. Trung, N.-E. Lee, *Adv. Mater.* **2016**, *28*, 4338.
- [48] Y. Yan, Z. Hu, Z. Yang, W. Yuan, C. Song, J. Pan, Y. Shen, *Sci. Rob.* **2021**, *6*, eabc8801.

- [49] X. Guo, W. Hong, T. Zhang, H. Li, T. Zhu, Q. Hong, D. Wang, L. Liu, Y. Zhao, D. Wang, Z. Mai, M. Wang, F. Yan, Y. Meng, Y. Xu, G. Xing, *Adv. Mater. Technol.* **2023**, *8*, 2201439.
- [50] H. Zhao, K. O'Brien, S. Li, R. F. Shepherd, *Sci. Rob.* **2016**, *1*, eaai7529.
- [51] W. Zhuang, G. Sun, H. Li, X. Lou, M. Dong, L. Zhu, *Optik* **2018**, *165*, 7.
- [52] T. Kim, S. Lee, T. Hong, G. Shin, T. Kim, Y.-L. Park, *Sci. Rob.* **2020**, *5*, eabc6878.
- [53] H. Souri, H. Banerjee, A. Jusufi, N. Radacsi, A. A. Stokes, I. Park, M. Sitti, M. Amjadi, *Adv. Intell. Syst.* **2020**, *2*, 2000039.
- [54] S. T. Frey, A. B. M. T. Haque, R. Tutika, E. V. Krotz, C. Lee, C. B. Haverkamp, E. J. Markvicka, M. D. Bartlett, *Sci. Adv.* **2023**, *8*, eabq1905.
- [55] E. Shahabi, F. Visentin, A. Mondini, B. Mazzolai, *Adv. Intell. Syst.* **2023**, *5*, 2200201.
- [56] B. Aksoy, Y. Hao, G. Grasso, K. M. Digumarti, V. Cacucciolo, H. Shea, *Nat. Commun.* **2022**, *13*, 4649.
- [57] Q. Guo, X. Zhang, *Composites, Part B* **2021**, *227*, 109434.
- [58] B. Mosadegh, P. Polygerinos, C. Keplinger, S. Wennstedt, R. F. Shepherd, U. Gupta, J. Shim, K. Bertoldi, C. J. Walsh, G. M. Whitesides, *Adv. Funct. Mater.* **2014**, *24*, 2163.
- [59] J. Hughes, U. Culha, F. Giardina, F. Guenther, A. Rosendo, F. Iida, *Front. Rob. AI* **2016**, *3*, 69.
- [60] G.-Z. Yang, J. Bellingham, P. E. Dupont, P. Fischer, L. Floridi, R. Full, N. Jacobstein, V. Kumar, M. McNutt, R. Merrifield, B. J. Nelson, B. Scassellati, M. Taddeo, R. Taylor, M. Veloso, Z. L. Wang, R. Wood, *Sci. Rob.* **2018**, *3*, eaar7650.
- [61] B. Mazzolai, C. Laschi, *Sci. Rob.* **2020**, *5*, eaba6893.
- [62] G. Giordano, M. Gagliardi, Y. Huan, M. Carlotti, A. Mariani, A. Menciassi, E. Sinibaldi, B. Mazzolai, *Adv. Sci.* **2021**, *8*, 2100418.
- [63] A. Constantinescu, A. M. Korsunsky, O. Pison, A. Oueslati, *Int. J. Solids Struct.* **2013**, *50*, 2798.
- [64] V. L. Popov, E. Willert, M. Heß, *Facta Univ., Ser.: Mech. Eng.* **2018**, *16*, 99.
- [65] A. M. Korsunsky, A. Constantinescu, *Thin Solid Films* **2009**, *517*, 4835.
- [66] D. Xu, T. Harvey, E. Begiristain, C. Domínguez, L. Sánchez-Abella, M. Browne, R. B. Cook, *J. Mech. Behav. Biomed. Mater.* **2022**, *133*, 105329.
- [67] Z. Wang, A. A. Volinsky, N. D. Gallant, *J. Appl. Polym. Sci.* **2015**, *132*, <https://doi.org/10.1002/app.41384>.
- [68] M. Tricarico, A. Papangelo, A. Constantinescu, M. Ciavarella, *Facta Univ.* **2019**, *17*, 95.
- [69] L. D. C. de Castro, L. Scabini, L. C. Ribas, O. M. Bruno, O. N. Oliveira, *Expert Syst. Appl.* **2023**, *212*, 118792.
- [70] V. Cacucciolo, H. Shea, G. Carbone, *Extreme Mech. Lett.* **2022**, *50*, 101529.
- [71] K. C. Galloway, K. P. Becker, B. Phillips, J. Kirby, S. Licht, D. Tchernov, R. J. Wood, D. F. Gruber, *Soft Rob.* **2016**, *3*, 23.
- [72] R. K. Katzschmann, J. DelPreto, R. MacCurdy, D. Rus, *Sci. Rob.* **2018**, *3*, eaar3449.
- [73] Y. Huan, I. Tamadon, C. Scatena, V. Cela, G. A. Naccarato, A. Menciassi, E. Sinibaldi, *IEEE Trans. Biomed. Eng.* **2020**, *68*, 56.
- [74] B. Mazzolai, A. Mondini, F. Tramacere, G. Ricconi, A. Sadeghi, G. Giordano, E. Del Dottore, M. Scaccia, M. Zampato, S. Carminati, *Adv. Intell. Syst.* **2019**, *1*, 1900041.
- [75] J. Park, Y. Lee, S. Cho, A. Choe, J. Yeom, Y. G. Ro, J. Kim, D. Kang, S. Lee, H. Ko, *Chem. Rev.* **2024**, *124*, 1464.
- [76] G. R. Gossweiler, G. B. Hewage, G. Soriano, Q. Wang, G. W. Welshofer, X. Zhao, S. L. Craig, *ACS Macro Lett.* **2014**, *3*, 216.
- [77] G. R. Gossweiler, T. B. Kouznetsova, S. L. Craig, *J. Am. Chem. Soc.* **2015**, *137*, 6148.
- [78] R. B. N. Scharff, J. Wu, J. M. P. Geraedts, C. C. L. Wang, in *2019 2nd IEEE Int. Conf. on Soft Robotics (RoboSoft)*, Seoul, South Korea **2019**, pp. 265–270.